Journal of Colloid and Interface Science 699 (2025) 138240

Contents lists available at ScienceDirect

Journal of Colloid And Interface Science

journal homepage: www.elsevier.com/locate/jcis

Interlayer-engineered MXene Nanosheets confining CoGa-LDH enable ultrafast charge transfer kinetics for high-energy potassium-ion supercapacitors

Chenxi Li [a], Mai Li [a,*], Xiang Peng [b], Inaam Ullah [a], Haotian Hu [a], Jiayi Shen [a], Ayesha Irfan [a], Wendong Xu [a], Paul K. Chu [c]

[a] College of Physics, Donghua University, Shanghai 201620, China
[b] Hubei Key Laboratory of Plasma Chemistry and Advanced Materials, Engineering Research Center of Phosphorus Resources Development and Utilization of Ministry of Education, School of Materials Science and Engineering, Wuhan Institute of Technology, Wuhan 430205, China
[c] Department of Physics, Department of Materials Science and Engineering, and Department of Biomedical Engineering, City University of Hong Kong, Tat Chee Avenue, Kowloon, Hong Kong, China

HIGHLIGHTS

- MXene-LDH synergy boosts charge kinetics, enhancing potassium-ion supercapacitors.
- Co_1Ga_1-LDH/MXene shows ultra-fast charge redistribution for high energy density.
- Composite achieves 85.2 % retention after 6000 cycles at 5 A/g current density.
- ASC device delivers 77.44 Wh/kg with excellent cycling stability.
- DFT analysis reveals optimal potassium adsorption and enhanced electronic states.

GRAPHICAL ABSTRACT

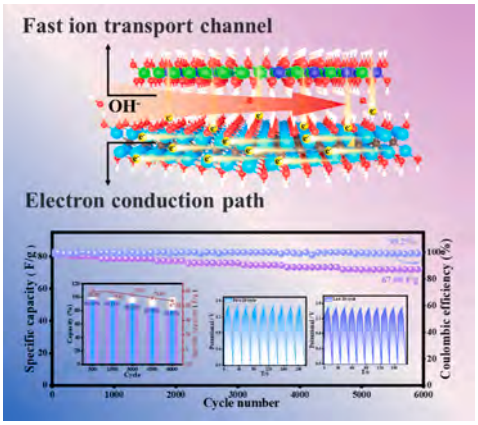

ARTICLE INFO

Keywords:
MXene
Layered double hydroxides
Hydrothermal synthesis
Potassium storage
Density functional theory

ABSTRACT

Two-dimensional MXenes, with their accordion-like morphology and facile exfoliation into monolayers, offer an ideal platform for immobilizing electroactive materials. However, composites fabricated from MXenes through conventional methods exhibit inhomogeneous dispersion, sluggish charge redistribution, and poor interfacial coupling, limiting their potassium-ion storage performance. Herein, an interlayer-engineered CoGa-LDH/MXene heterostructure is fabricated via Peltier effect-driven rotational hydrothermal synthesis with tunable Co/Ga ratios. This approach ensures atomic-level confinement of layered double hydroxide (LDH) within MXene interlayers while strengthening interfacial coupling and ion transport kinetics. The resulting heteroarchitecture synergizes the high pseudocapacitance of CoGa-LDH and the metallic conductivity of MXene, enabling ultrafast

* Corresponding author.
E-mail address: limai@dhu.edu.cn (M. Li).

https://doi.org/10.1016/j.jcis.2025.138240
Received 19 April 2025; Received in revised form 16 June 2025; Accepted 17 June 2025
Available online 18 June 2025

ion/electron transport and suppressing self-aggregation. Optimized Co_1Ga_1-LDH/MXene delivers a remarkable specific capacitance of 1345.3 F/g and exceptional cyclability (85.13 % retention after 6000 cycles), surpassing most reported LDH-based supercapacitors. Density functional theory (DFT) calculations reveal that the heterointerface enhances K^+-ion adsorption energy and modulates charge distribution, accelerating redox kinetics. When the Co_1Ga_1-LDH/MXene composite is assembled into an asymmetric supercapacitor (ASC), the device achieves an energy density of 77.4 Wh/kg at 1125 W/kg, with sustained performance under rigorous cycling. This work elucidates the confinement engineering of MXene-based compounds and their potassium storage mechanisms, providing critical references for high-energy-density supercapacitors in alkaline systems.

1. Introduction

The urgent need to transition from fossil fuels to sustainable energy systems has intensified the demand for electrochemical energy storage (EES) devices that integrate high energy density, rapid charge/discharge kinetics, and long-term cyclability [1,2]. Supercapacitors (SCs), bridging the gap between conventional batteries and capacitors, have emerged as leading candidates for high-power applications [3], from regenerative braking to grid-frequency regulation, due to their millisecond-scale response and virtually unlimited cycle life [4]. However, their widespread adoption in energy-intensive domains such as electric vehicles and portable electronics remains hindered by inherently low energy densities, a limitation rooted in the physical charge-storage mechanisms of traditional electrode materials [5]. To overcome this barrier, the scientific community has shifted focus toward advanced electrode architectures that synergize faradaic and non-faradaic processes, unlocking unprecedented energy-power performance [6].

Significant research efforts have been devoted to developing advanced electrode materials for potassium-ion supercapacitors [7], with four major material categories including defect-engineered chalcogenides (e.g., WS_2Se_{2-x}) [8], Mn-based Prussian blue analogs (e.g., $K_{1.86}Mn[Fe(CN)_6]_{0.96}\cdot 19H_2O$) [9], metal-organic frameworks (e.g., $[Zn_2(BDC)_2DABCO]_n$) [10,11], and alloy-based cathodes [12]. Despite these advances, mainstream potassium-ion storage systems still face critical challenges, including sluggish potassium-ion insertion/extraction kinetics and electrode degradation during cycling [13,14]. Overcoming these limitations requires strategic material design that balances high electronic conductivity, expansive ion-accessible surfaces, and ultrafast redox kinetics to unlock the full potential of potassium-ion energy storage for practical applications [15].

Among pseudocapacitive materials, layered double hydroxides (LDH) stand out for their anion-exchange capacity, tailorable redox chemistry, and structural versatility [16,17]. Their general formula $[M_{1-x}^{2+}M_x^{3+}(OH)_2]^{2+}$ (where M^{2+} and M^{3+} are bivalent/trivalent cations and A^{n-} denotes interlayer anions) enables atomic-level tuning of electronic and ionic transport properties through cationic ratio optimization [18,19]. The ratios of bivalent and trivalent cations in bimetallic hydroxides, along with their crystal structures, critically influence morphology and capacitive properties [20]. By adjusting the metal ion ratio, bimetallic LDH materials achieve high specific capacity, improved cycling stability, and enhanced conductivity. Consequently, rational design and optimization of metal ion ratios have become key strategies to advance supercapacitor performance [21]. According to the foundational role of conventional transition metal ions such as Co^{2+}, Fe^{3+}, and Ni^{2+} in LDH electrode architectures [22], recent advancements in group IIIA metal integration, notably the gallium cation (Ga^{3+}), have unveiled novel avenues to enhance the electrochemical performance [23]. The ≈ 368 kJ/mol Ga-O bond energy, surpassing that of Ni—O (280 kJ/mol) and Co—O (305 kJ/mol), reduces lattice distortion during cycling and improves the specific capacity [24,25]. The introduction of Ga enhances the LDH electrical conductivity by equivalent substitution of metal ions such as Ni^{2+} and Co^{2+} [26]. For instance, Liu et al. demonstrated $NiGa_2O_4$ electrodes achieving 1508 F/g at 1 A/g, 63.7 % capacitance retention at 20 A/g, and 102.4 % capacity retention after 10,000 cycles, showcasing potential of gallium to stabilize high-capacity electrodes [27]. Although Ga^{3+} modifies the conductivity of LDH [28], the nanoparticle coalescence tendency and residual charge transfer resistance hamper high-power-density supercapacitor applications [29]. Despite their advantages, Ga^{3+}-modified LDHs still face particle aggregation and sluggish kinetics, necessitating conductive scaffolds to maximize pseudocapacitive performance [30].

MXenes, a class of two-dimensional transition-metal carbides and nitrides such as $Ti_3C_2T_x$, are endowed with metallic conductivity approaching 6000 S/cm, hydrophilic surfaces, and mechanically robust interlayer galleries [31]. Unlike graphene derivatives, MXenes uniquely combine high redox-active surface sites with rapid ion-diffusion pathways, making them ideal substrates for hosting layered double hydroxides. However, inherent oxidative instability and self-stacking compromise the performance of standalone MXene electrodes [32]. To address this, researchers have developed multilayered MXenes with accordion-like morphologies through MAX phase etching with chemical and thermal treatments, followed by ultrasonic exfoliation to yield monolayer nanosheets [33]. These monolayers serve as excellent substrates for active material immobilization. In composite architectures, MXene provides synergistic advantages including large surface area and high conductivity [34]. Previous studies have demonstrated the feasibility of LDH/MXene composites for enhanced energy storage. For example, Zhao and colleagues used liquid phase deposition and electrostatic self-assembly to stack $Ti_3C_2T_x$ and nickel-cobalt-aluminum LDH nanosheets, forming a heterostructure with specific capacitance of 748.2 F/g at 1 A/g [35,36]. Similarly, Zhang and coworkers synthesized iron-nickel LDH/$Ti_3C_2T_x$-MXene composites by assembling iron-nickel LDH on two-dimensional $Ti_3C_2T_x$ nanosheets, constructing a symmetric supercapacitor with energy density of 94.1 Wh/kg at 7431.8 W/kg [37]. However, these composites still lack atomic-level interfacial control, resulting in inefficient charge redistribution and limited rate capability [38,39].

Our strategy leverages the structural synergy between cobalt-gallium LDH and MXene to overcome limitations of conventional composites. Through a Peltier effect-driven rotational hydrothermal method, we achieve confined growth of cobalt-gallium LDH within MXene interlayers, creating a robust cobalt-oxygen-gallium bonding network that ensures uniform dispersion and strong interfacial coupling. This heterostructure capitalizes on conductive highways of MXene and redox-active sites of LDH, enabling ultrafast potassium-ion diffusion while suppressing electrode degradation. Systematic optimization of cobalt to gallium ratios shows the Co_1Ga_1-LDH/MXene composite achieves a specific capacitance of 1345.3 F/g and maintains 85.13 % capacity retention after 6000 cycles. Density-functional theory (DFT) calculations confirm enhanced potassium-ion adsorption energy (−2.36 eV) and modified electronic structure at the heterointerface, collectively accelerating charge storage kinetics. When configured into an asymmetric supercapacitor with Co_1Ga_1-LDH/MXene as positive electrode and activated carbon as negative electrode, the device achieves high energy density of 77.4 Wh/kg at 1125 W/kg and demonstrates practical viability by powering commercial electronics within seconds. This work not only advances MXene-based heterostructure design but also provides a universal platform for next-generation high-energy storage systems.

2. Experimental details

2.1. Materials

Gallium nitrate trihydrate ($Ga(NO_3)_3{\cdot}xH_2O$, analytical grade) and cobalt nitrate hexahydrate ($Co(NO_3)_2{\cdot}6H_2O$, analytical grade) were supplied by Shanghai Maclin Biochemical Co., Ltd. Hydrofluoric acid (HF, analytical grade) was obtained from GENERAL-REAGENT. Absolute ethanol (analytical grade) was acquired from Aladdin Biochemical Technology Co., Ltd. (Shanghai). Titanium aluminum carbide (Ti_3AlC_2, 98 % purity, analytical grade) was provided by Foshan Xinxi Technology Co., Ltd. All the reagents were used without additional purification. Deionized water (resistivity ≥18.2 MΩ·cm) was employed throughout the experiments.

2.2. Preparation of MXenes

10 mL of 12 M HCl was combined with 0.8 mL of HF in a 60 mL polypropylene bottle and stirred for 5 min. 1 g of Ti_3AlC_2 powder was added slowly to the acidic mixture under stirring to mitigate the exothermic reaction. The mixture was transferred to a temperature-controlled magnetic stirrer and reacted at 35 °C for 24 h to selectively etch the Al layers from Ti_3AlC_2 [40]. The suspension was centrifuged at 5200 rpm for 10 min. The acidic supernatant was discarded, and the residue was washed repeatedly with deionized water until the pH reached 6–7. The sediment was collected by vacuum filtration through a 0.22-μm polypropylene membrane, re-dispersed in 150 mL deionized water via filter cake sonication for 1 h. The exfoliated MXene suspension was lyophilized at −50 °C for 24 h to obtain delaminated MXene flakes for subsequent use.

2.3. Preparation of Co_xGa_y-LDH/MXene

The multilayered MXene powder (10 mg) was dispersed in 10 mL of anhydrous ethanol and exfoliated by bath sonication for 30 min to obtain a colloidal suspension. The MXene suspension was introduced into 30 mL of ethanol containing 100 mg $Co(NO_3)_2{\cdot}6H_2O$ and 100 mg $Ga(NO_3)_3{\cdot}xH_2O$ and stirred magnetically for 20 min. The mixture underwent a hydrothermal treatment at 80 °C for 10 h in a Teflon-lined autoclave under continuous stirring at 5000 rpm. After cooling, the product was transferred to a conventional Teflon-lined autoclave and subjected to secondary hydrothermal treatment at 180 °C for 3 h under static conditions. The precipitate was collected by centrifugation (8000 rpm, 10 min), washed repeatedly with deionized water until the supernatant reached a neutral pH, and then freeze-dried for 12 h to obtain the final product. Three composites with Co:Ga molar ratios of 1:1, 1:0.5, and 1:0 were prepared by adjusting the $Ga(NO_3)_3{\cdot}xH_2O$ mass to 100 mg, 50 mg, and 0 mg (with.

$Co(NO_3)_2{\cdot}6H_2O$ fixed at 100 mg), denoted as Co_xGa_y-LDH/MXene (x and y represent the mass ratio of Co:Ga precursors). With the amount of $Co(NO_3)_2{\cdot}6H_2O$ kept unchanged and no Ga source or MXene added, the hydrothermal and post-treatment steps were repeated to obtain pure-phase Co-LDH as a control. All samples were preserved for subsequent physicochemical and electrochemical characterizations.

2.4. Preparation of electrodes

The working electrode (WE) was prepared by the slurry coating method with pre-cleaned nickel foam (NF, 1 × 1 cm^2) as the current collector. The electrode pastes, consisting of 80 wt% active substance, 10 wt% polyvinylidene fluoride (PVDF) binder, and 10 wt% conductive carbon black (Super P), was dissolved in *N*-methyl-2-pyrrolidone (NMP) and stirred at 500 rpm for 1 h to ensure uniform dispersion. Subsequently, the slurry was evenly coated on the NF substrate, and the loaded amount was about 2 mg/cm^2. The coated electrodes were vacuum-dried at 80 °C for 6 h to enhance the interface contact between the active materials and the collector. In this structure, PVDF acts as a chemically stable polymer binder to ensure that the active substance is firmly attached to the NF collector and maintains the integrity of the electrode structure during cycling. Super P builds a conductive network to alleviate the insulation characteristics of PVDF and reduce the internal resistance of the electrode. In the ASC, the composite electrode is used as the positive electrode, and the negative electrode is prepared by the same process using a slurry composed of 80 wt% AC, 10 wt% Super P, and 10 wt% PVDF. The CHI660E electrochemical workstation was used to evaluate the potassium storage characteristics of the electrode.

3. Results and discussion

Fig. 1a depicts the stepwise synthesis of Co_xGa_y-LDH/MXene composites. Initially, multilayered $Ti_3C_2T_x$ MXene was synthesized via HCl/HF selective etching of Al layers from Ti_3AlC_2, effectively expanding the interlayer spacing. Subsequently, controlled nucleation of Co_xGa_y-LDH was achieved through the introduction of Co^{2+} and Ga^{3+} precursors under alkaline conditions, followed by a one-pot hydrothermal process that uniformly anchored LDH nanostructures onto MXene sheets. This integrated approach synergistically combines the structural openness of MXene with the redox-active sites of LDH, establishing interconnected ion-diffusion channels and conductive electron-transfer pathways to significantly enhance electrochemical energy storage performance. As shown in Fig. 1b and c, the expended MXene interlayer facilitates ultrafast diffusion channels for OH^- and K^+ ions. The metallic conductivity of MXene establishes a high-speed electron transport network, compensating for the poor electrical conductivity of Co_1Ga_1-LDH. The introduction of Ga^{3+} induces oxygen vacancies through charge compensation effects, and these vacancies function as highly active sites in redox reactions. In parallel, the negatively charged functional groups (–F/–OH) on the MXene surface selectively attract K^+, generating electrical double-layer capacitance which synergistically combines with the Faradaic pseudocapacitance of the LDH, collectively enabling both high power density and high energy density [41].

The scanning electron microscopy (SEM) images acquired at different magnifications reveal morphological evolution. Fig. 2a and b display the pristine multilayer MXene with irregular nanosheet dimensions and sporadic surface particulates under low- and high-magnifications, respectively. In comparison, Co_1Ga_1-LDH/MXene (Fig. 2c and d) shows uniformly anchored LDH nanoparticles on the MXene surface and interlayers, with significantly denser deposition than observed in the $Co_1Ga_{0.5}$-LDH/MXene and Co_1Ga_0-LDH/MXene counterparts (Fig. S1). This optimized architecture not only mechanically stabilizes the MXene framework against restacking but also maximizes electrochemically active interfaces through homogeneous LDH distribution [42].

The hierarchical architecture of the Co_1Ga_1-LDH/MXene composite was verified by transmission electron microscopy (TEM). As shown in Fig. 2e, low-magnification TEM reveals uniform deposition of Co_1Ga_1-LDH nanoparticles across the MXene sheets and close attachment to the basal planes and interlayer spaces. The high-resolution TEM image (Fig. 2f) shows a polycrystalline structure at the MXene-Co_1Ga_1-LDH interface, where lattice spacings of 0.155 nm and 0.382 nm, corresponding to the (110) and (006) planes of Co_1Ga_1-LDH, respectively, and a lattice spacing of 0.263 nm corresponds to the (101) plane of MXene. The cross-sectional imaging in Fig. 2g demonstrates the preservation of lamellar stacking with LDH-intercalated MXene layers, consistent with SEM observations. Atomic-scale analysis of the boxed region in Fig. 2g, presented in Fig. 2h, resolves coexisting lattice fringes of 0.259 nm attributable to the (012) plane of Co_1Ga_1-LDH alongside MXene signatures, corroborating seamless integration on the atomic level. The SAED pattern (Fig. 2g) reveals diffraction rings corresponding to the (014), (100), (106), and (1011) crystal faces (red circles) of MXene, and the (015) and (110) crystal faces (yellow circles) representing Co_1Ga_1-LDH. The elemental maps in Fig. 2i (i_1, i_2, i_3, i_4, i_5)

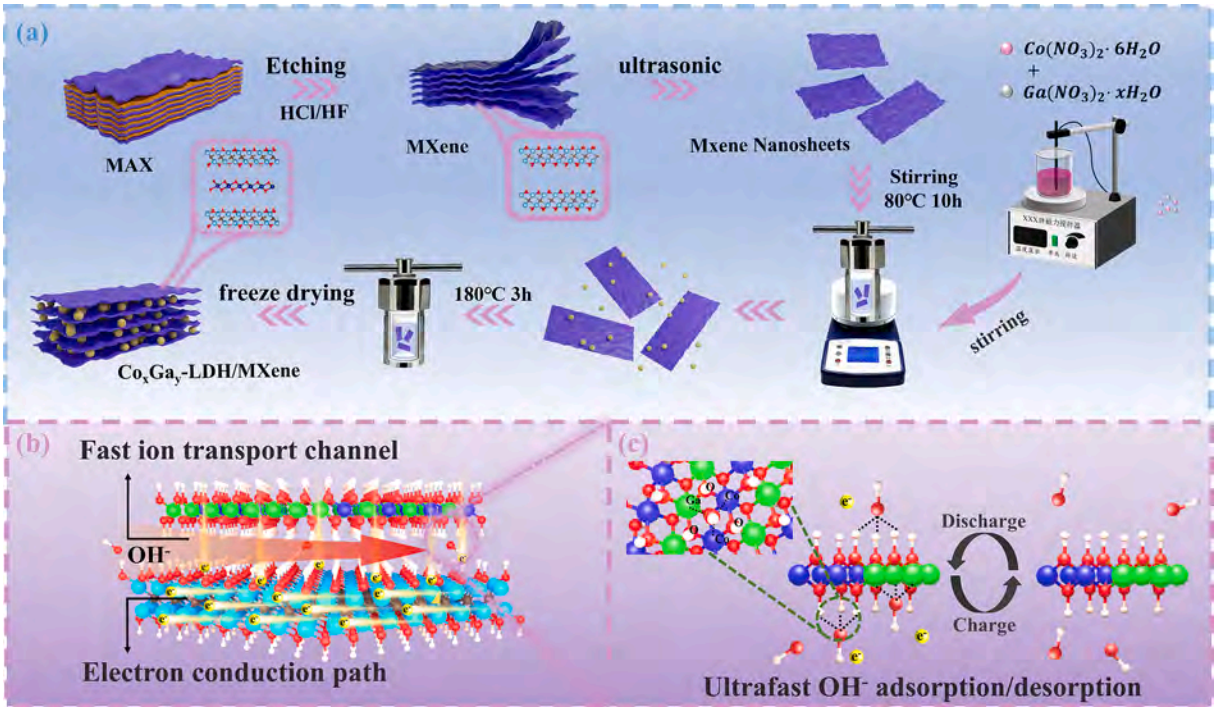

Fig. 1. (a) Schematic illustration of the preparation of Co_xGa_y-LDH/MXene composites; (b) Schematic of the charge storage mechanism in Co_1Ga_1-LDH/MXene; (c) Schematic diagram of redox reaction.

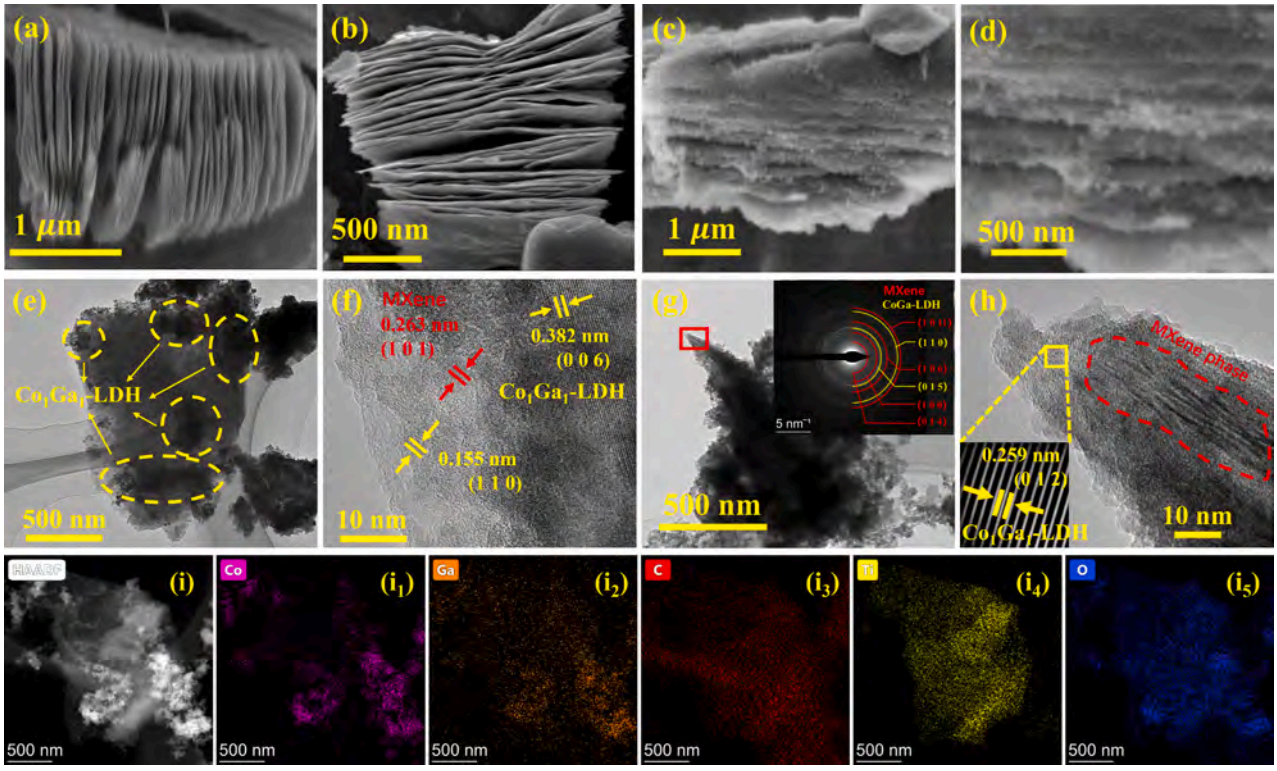

Fig. 2. SEM images of (a, b) $Ti_3C_2T_x$ MXene and (c, d) Co_1Ga_1-LDH/MXene at different magnifications; (e, f, g, h) TEM images of Co_1Ga_1-LDH/MXene at various magnifications and SAED patterns; (i-i_5) Elemental maps of Co, Ga, C, Ti, and O.

confirms even distributions of Ti, Ga, Co, and O, indicating uniform dispersion of Co_1Ga_1-LDH on MXene.

To characterize the crystal structure and phases, X-ray diffraction (XRD) was performed. As shown in Fig. 3a, the XRD spectra of the synthesized Co-LDH, MXene and its composites (Co_1Ga_0-LDH/MXene, $Co_1Ga_{0.5}$-LDH/MXene, and Co_1Ga_1-LDH/MXene) reveal distinct phase signatures. For Co_1Ga_1-LDH/MXene and $Co_1Ga_{0.5}$-LDH/MXene diffraction peaks at 2θ values of 11.92°, 17.98°, 30.24°, and 38.5° (marked

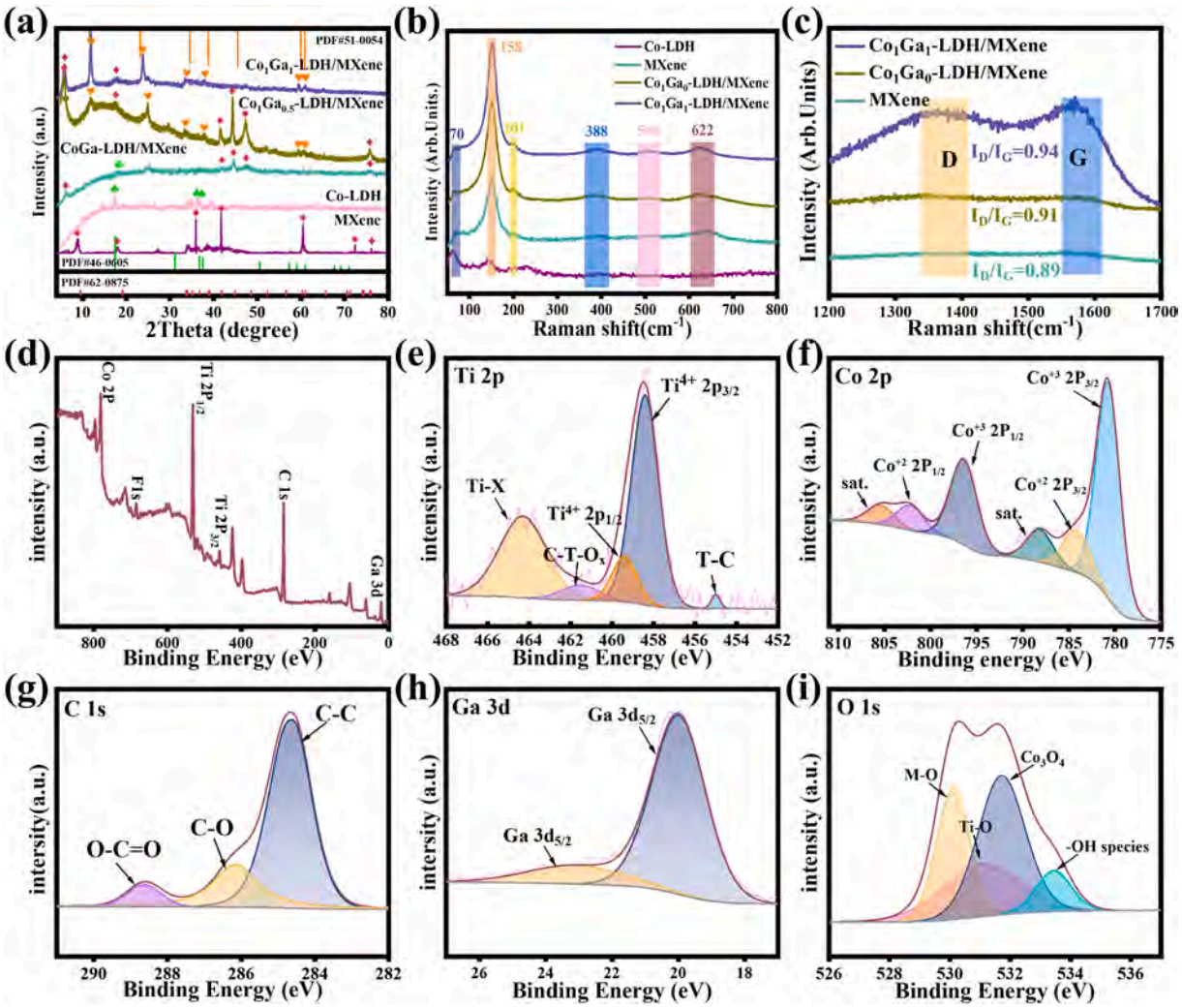

Fig. 3. (a) XRD patterns of Co-LDH, MXene, Co_1Ga_0-LDH/MXene, $Co_1Ga_{0.5}$-LDH/MXene, and Co_1Ga_1-LDH/MXene; (b, c) Raman scattering spectra of Co-LDH, MXene, Co_1Ga_1-LDH/MXene, and Co_1Ga_0-LDH/MXene; (d) XPS survey spectrum of Co_1Ga_1-LDH/MXene; High-resolution XPS spectra of (e) Ti 2p, (f) Co 3d, (g) C 1 s, (h) Ga 2p and (i) O 1 s.

with orange heart symbols) correspond to the (003), (006), (009), and (015) planes of CoGa-LDH (PDF#51–0045) respectively, which are consistent with previous studies. Characteristic peaks of MXene (PDF#52–0875) appear at $2\theta = 5.9°$ and 17.81° and broader diffraction peaks (marked by red diamonds) exhibit its laminated structure [43]. Notably, the MXene peak intensities in Co_1Ga_1-LDH/MXene are significantly attenuated compared to those in $Co_1Ga_{0.5}$-LDH/MXene, suggesting enhanced structural disorder with increasing Ga^{3+} doping concentration. XRD analysis further indicates successful incorporation of CoGa-LDH nanoparticles into the interlayer space of MXene. Pure Co-LDH displays sharp diffraction peaks (PDF#30–0443), confirming high crystallinity. In contrast, Co_1Ga_0-LDH/MXene exhibits only weak peaks, implying amorphous or low-crystallinity characteristics [44].

The Raman spectra (RS) were performed to characterize molecular vibrations, with spectra shown in Fig. 3b. For pure Co-LDH, the sharp peak at 61 cm^{-1} is assigned to translational vibration of the Co—O lattice, while peaks at 139 cm^{-1} and 229 cm^{-1} arisefrom the bending vibration of the Co–OH bond and the restricted vibration of the interlayer water molecules, confirming typical lamellar double hydroxide structure [45]. The characteristic Raman band of $Ti_3C_2T_x$ MXene at 158 cm^{-1} corresponds to Ti—C vibration and terminal surface moieties (e.g., —O, –OH and —F). Additional vibrational modes include the A_{1g} mode at 201 cm^{-1} and E_x mode at 388 cm^{-1}, with higher-frequency modes at 506 cm^{-1} (A_{1g} mode) and 622 cm^{-1} (E_x mode) attributed to C-Ti-OH vibration. For the Co_1Ga_0-LDH/MXene and Co_1Ga_1-LDH/MXene composites, the RS retains MXene-phase features [46]. Notably, the Raman band of Co_1Ga_1-LDH/MXene exhibits a slight redshift relative to pristine MXene, indicating interfacial coupling between MXene and CoGa-LDH. As shown in Fig. 3c, the carbon vibrational modes at 1390 cm^{-1} (D band) and 1590 cm^{-1} (G band) show an intensity ratio (I_D/I_G) indicating for the graphitic crystallinity and defect density. The Co_1Ga_1-LDH/MXene composite shows a significantly higher ratio (0.94) than pristine MXene (0.89) [47], suggesting that the incorporation of CoGa-LDH with MXene introduces additional defects, that likely amplifies the exposure of charge-transfer sites for enhanced reactivity.

XPS was conducted to determine the oxidation states and interfacial interactions in Co_1Ga_1-LDH/MXene nanocomposites. The survey spectrum (Fig. 3d) confirms the coexistence of Co/Ga from LDH and C/Ti/O/F from MXene. The Ti 2*p* spectrum (Fig. 3e) reveals five states by Gaussian-Lorentzian fitting. The Ti—C covalent bonding peaks at 454.6 eV and 458.2 eV indicate the presence of $Ti_3C_2T_x$, consistent with previous reports [48]. The Ti^{4+} states at 458.4 eV ($2p_{3/2}$) and 459.4 eV ($2p_{1/2}$) indicate surface oxidation without crystalline TiO_2 formation, as evidenced by the absence of TiO_2 XRD peaks. The C–Ti–O_x configuration at 464.3 eV demonstrates MXene surface functionalization (–O/–OH groups), enabling LDH anchoring through Ti–O–M bonds (M = Co/Ga). Replacement MAX-phase Al with –OH/–F surface groups enable covalent integration of CoGa-LDH into MXene via Ti–O–M bonds (M = Co/

Ga), which stabilizes surface Ti against oxidation and establishes synergistic interfacial adhesion through oxygen-bridged chemical bonding, enhancing charge transfer and structural stability. The Co 2*p* spectrum (Fig. 3f) exhibits $2p_{3/2}$-$2p_{1/2}$ doublets at 780.9/796.5 eV (Co^{3+}) with satellite peaks at 784.4/802.4 eV (Co^{2+}), confirming mixed cobalt oxidation states [49]. The C 1 *s* spectrum in Fig. 3g reveals three main peaks at 284.6 eV, 286.2 eV, and 288.6 eV, corresponding to Ti—C, C—C, and O–C=O, respectively. In the Ga 3*d* spectrum (Fig. 3h), the two peaks at 19.56 eV and 20.41 eV are assigned to Ga $3d_{5/2}$ and Ga $3d_{3/2}$, further confirming the presence of Ga—O 1 *s* and Ga—O 2 *s* bonds in Co_1Ga_1-LDH. The O 1 *s* spectrum (Fig. 3i) shows metal-oxygen bonds (M–O at 528.9 eV, M = Co/Ga), Ti–O–C (530.8 eV), hydroxyl groups (532.7 eV), and residual carbonate (535.3 eV), confirming LDH-MXene interfacial bonding [50].

To explore the impact of gallium (Ga) doping on the electrode properties, DFT calculations were carried out. Fig. 4a-c illustrates the atomic models of pristine MXene, Co_1Ga_0-LDH/MXene, and Co_1Ga_1-LDH/MXene during K^+ adsorption. The adsorption energetics in Fig. 4d follow a descending order: −0.68 eV (MXene), −1.67 eV (Co_1Ga_0-LDH/MXene), and − 2.36 eV (Co_1Ga_1-LDH/MXene). Notably, the Co_1Ga_1-LDH/MXene achieves the lowest adsorption energy. This demonstrates an increased K^+ adsorption capacity and accelerated storage/release kinetics, indicating that Ga doping enhances the ion adsorption efficiency, particularly K^+ storage and release. The electronic transport

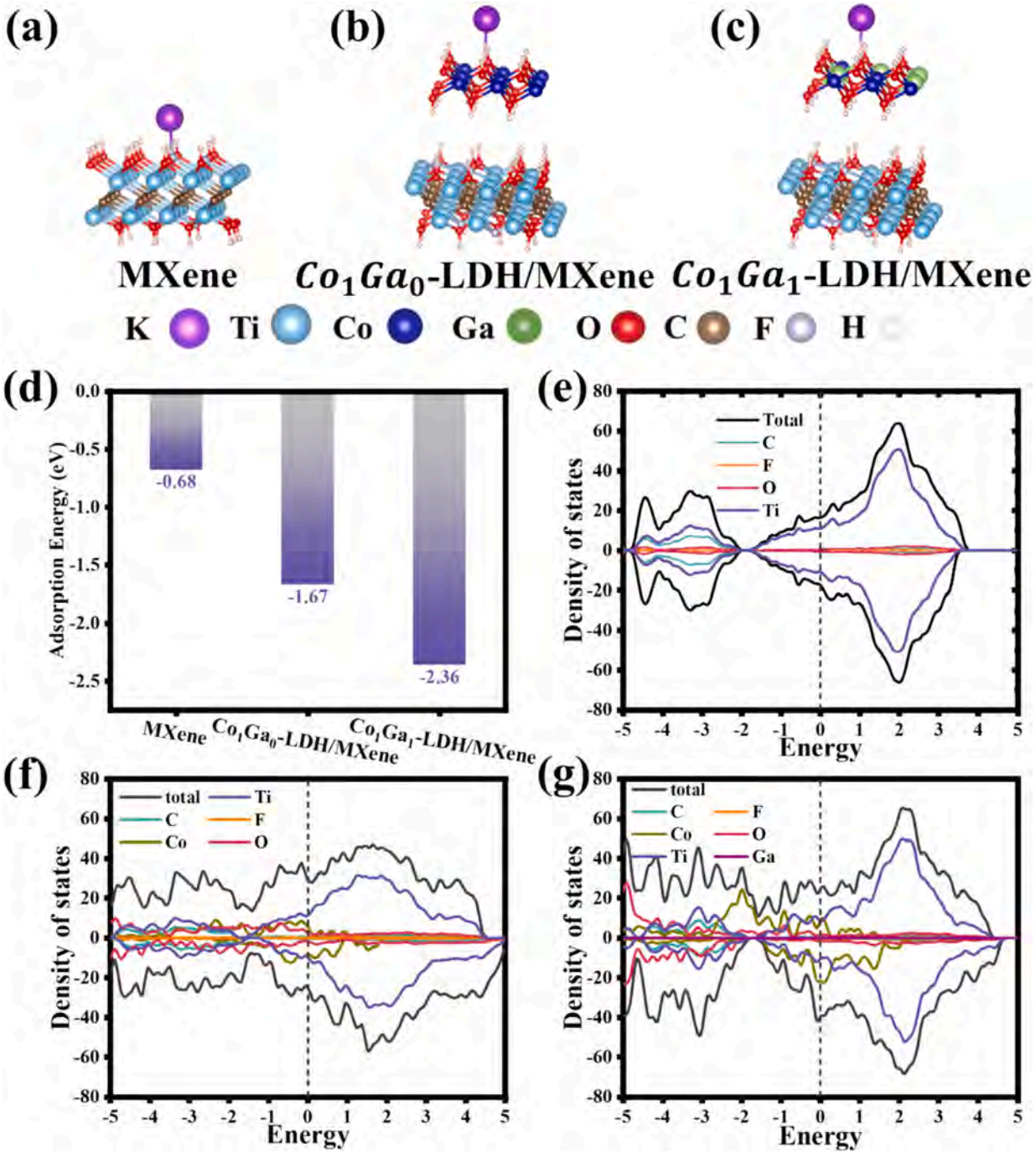

Fig. 4. Chemical structures of (a) MXene, (b) Co_1Ga_0-LDH/MXene, and (c) Co_1Ga_1-LDH/MXene; (d) Adsorption energies; DOS of (e) MXene, (f) Co_1Ga_0-LDH/MXene, and (g) Co_1Ga_1-LDH/MXene, where the dashed lines indicate the Fermi energy levels.

properties were assessed by the DOS, as shown in Fig. 4e-g. Co_1Ga_1-LDH/MXene shows significantly elevated DOS near the Fermi level, indicating improved conductivity, which is confirmed experimentally. As for the pristine MXene, the DOS near the Fermi level is dominated by Ti, whereas in Co_1Ga_0-LDH/MXene, strengthened Ti—Co coupling increases the Fermi-level DOS and oxygen-related electronic states through Co-mediated modulation of oxygen electronic states and enhances charge carrier delocalization and conductivity. Comparison of Co_1Ga_0-LDH/MXene and Co_1Ga_1-LDH/MXene DOS reveals that Ga doping strengthens Ga—Co coupling and elevates the Fermi-level DOS in the Co_1Ga_1-LDH/MXene. Ga doping also results in a 0.17 eV positive shift in the *d*-band center, from −1.84 eV for the undoped system to −1.67 eV for Co_1Ga_1-LDH/MXene. This modulation originates from the constructed Ga-doped Co–O–Ga network, which enhances hybridization between the Co 3*d* and Ga 4*p* orbitals. The resultant upward shift of the Co *d*-band center reduces the electron-leap potential, thereby enhancing the intrinsic conductivity.

The electrochemical properties of Co-LDH, MXene and Co_xGa_y-LDH/MXene were determined by cyclic voltammetry (CV) at 5 mV/s in 1 M KOH. As shown in Fig. 5a, the CV curve of Co-LDH electrode exhibits an anodic peak at 0.50 V and a cathodic peak at 0.43 V. For Co_1Ga_0-LDH/MXene electrode, the redox peaks appear at 0.50 V (anodic) and 0.35 V (cathodic). With increasing Ga content, $Co_1Ga_{0.5}$-LDH/MXene shows peaks shifting to 0.35 V (anodic) and 0.25 V (cathodic), while Co_1Ga_1-LDH/MXene further displays cathodically shifted peaks with anodic and cathodic peaks at 0.39 V and 0.20 V, respectively. These peak displacements indicate enhanced charge transfer kinetics due to Ga incorporation, attributed to reversible Co^{2+}/Co^{3+} and Ga^{3+}/Ga^{4+} transitions. Notably, the CV integral area of Co_1Ga_1-LDH/MXene electrode is 6.33 and 14.62 times larger than those of pristine MXene and Co-LDH. This enhancement originates from Ga-induced electronic modulation, which optimizes Co redox activity. Additionally, the presence of extra electroactive functional groups in the LDH-MXene heterostructure improves ion adsorption and interfacial charge storage. The electrochemical processes are shown in the following:

$$Co^{2+} + OH^- \Leftrightarrow Co^{3+} + -OH + e^- \quad (4)$$

$$Ga^{3+} + OH^- \Leftrightarrow Ga^{4+} + -OH + e^- \quad (5)$$

Galvanostatic charge/discharge (GCD) analysis at 1 A/g under

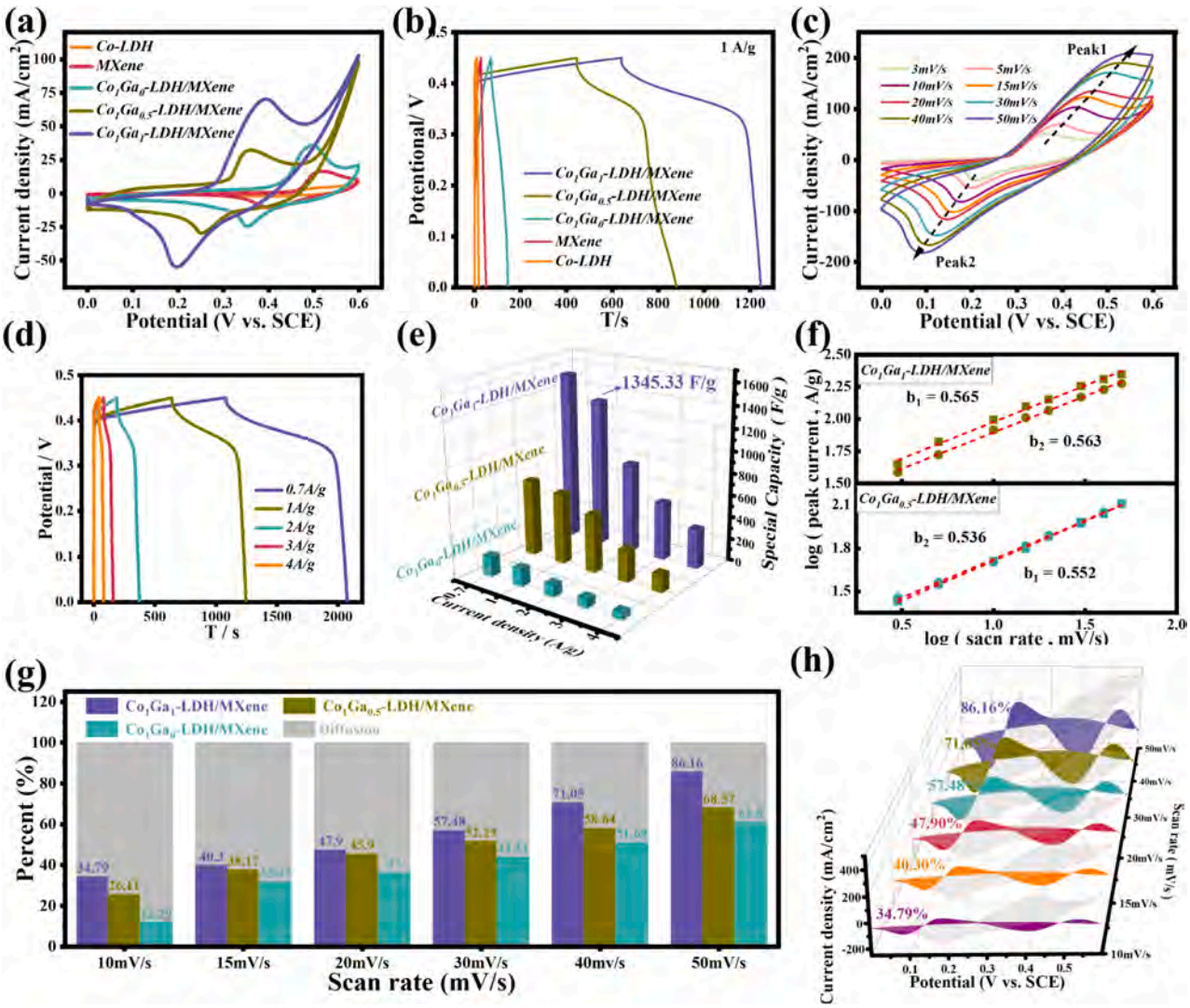

Fig. 5. Co-LDH, MXene, Co_1Ga_0-LDH/MXene, $Co_1Ga_{0.5}$-LDH/MXene and Co_1Ga_1-LDH/MXene: (a) CV curves at 5 mV/s; (b) GCD curves at a current density of 1 A/g; (c) CV curves at 3–50 mV/s; (d) GCD curves at different current densities of Co_1Ga_1-LDH/MXene; (e) Specific capacitances of Co_1Ga_0-LDH/MXene, $Co_1Ga_{0.5}$-LDH/MXene, and Co_1Ga_1-LDH/MXene for different current densities; (f) *b* value calculation using power law; (g) Contribution of Co_1Ga_0-LDH/MXene, $Co_1Ga_{0.5}$-LDH/MXene and Co_1Ga_1-LDH/MXene diffusion and capacitive processes; (h) Separation of the capacitive current of Co_1Ga_1-LDH/MXene electrode from the total current response at different scanning rates, with capacitance fractions shown in the shaded area.

0–0.45 V window (Fig. 5b) reveals Ga-dependent capacitive properties, showing specific capacitance of 14 F/g for Co-LDH, 50.7 F/g for MXene, 162.7 F/g for Co_1Ga_0-LDH/MXene, 644 F/g for $Co_1Ga_{0.5}$-LDH/MXene, and 1345.3 F/g for Co_1Ga_1-LDH/MXene. The Co_1Ga_1-LDH/MXene electrode exhibits the longest discharge duration and demonstrates the optimal charge storage capability. The Ga-dependent enhancement stems from that Ga^{3+}-induced oxygen vacancies increase ion adsorption sites and optimize the Ga/Co ratios, thus preventing MXene restacking by steric hindrance. CV analysis (Fig. 5c) reveals the redox characteristics of Co_1Ga_1-LDH/MXene electrodes under different scanning rates (1–50 mV/s) between 0 and 0.6 V. Fig. S2 and S3 show the electrochemical behavior of the samples with varying Co and Ga molar ratios. The anodic and cathodic peaks shift to higher and lower potentials, respectively, with increasing scanning rates, but the shape of the CV curves remains nearly unchanged, indicating superior charge transfer kinetics and near-ideal reversibility. Fig. 5d depicts the GCD profiles of Co_1Ga_1-LDH/MXene electrodes from 0.7 A/g to 4 A/g and indicates that the electrodes maintain good stability even at high current densities. The evolution of specific capacitance with increasing current density for all composite electrode materials is illustrated in Fig. 5e. At 0.7 A/g, the specific capacitances of Co-LDH, MXene, Co_1Ga_0-LDH/MXene, $Co_1Ga_{0.5}$-LDH/MXene, and Co_1Ga_1-LDH/MXene are 18 F/g, 64.7 F/g, 185.7 F/g, 692.5 F/g, and 1546.8 F/g, respectively, with the Co_1Ga_1-LDH/MXene electrodes exhibiting the highest capacitance. Fig. S4 shows that the Coulombic efficiency of Co_1Ga_1-LDH/MXene remains at 94.45 % at 1 A/g and improves to 99.03 % at 4 A/g. These findings confirm the simultaneous achievement of high capacitance retention and near-ideal charge transfer efficiency, and the dynamic interaction between electrolyte and the surface of the materials plays a crucial role in the electrochemical performance.

Tables S1-S3 summarize the charge transfer kinetics of MXene-based composites, LDH-based composites, and LDH/MXene hybrid electrodes [47,51–53]. Compared to recently reported specific capacitances, Co_1Ga_1-LDH/MXene exhibits competitive and even superior properties. The introduction of CoGa-LDH provides extra electrochemically active sites structurally stabilizes the interlayer framework of MXene for fast OH^- diffusion kinetics. Consequently, Co_1Ga_1-LDH/MXene exhibits significant advantage over other MXene-based materials.

Theoretically, the electrode capacitance is governed by two processes: the diffusion-controlled process (i_{diff}) driven by electrochemical transformations at the electrode surface/subsurface, and the capacitance-controlled process (i_{cap}) arising from reversible ion electrosorption at the electrode-electrolyte interface. In the CV test, the relationship between the scan rate (v) and the electrode current (i) can be described by the following equation:

$$i = i_{cap} + i_{diff} = av^b \tag{7}$$

$$\log i = \log a + b \log v \tag{8}$$

where v represents the scan rate and a and b are empirical constants. A b value close to 1 suggests that the electrochemical processes are primarily capacitively controlled, whereas a b value near 0.5 indicates that diffusion-controlled processes dominate. The equations provide a quantitative framework to assess the electrochemical behavior of the electrode for different potential scan rates. The b values, calculated from the relationship between the scan rate and peak current of the redox peaks, are used to analyze the charge storage characteristics of the Co_1Ga_1-LDH/MXene and $Co_1Ga_{0.5}$-LDH/MXene electrodes. As shown in Fig. 5f, the b values of the reduction and oxidation peaks of Co_1Ga_1-LDH/MXene are 0.565 and 0.563, respectively, whereas those of $Co_1Ga_{0.5}$-LDH/MXene are 0.552 and 0.536. The results indicate that the energy storage mechanism of Co_1Ga_1-LDH/MXene electrode involves both diffusion and capacitive effects. Specifically, higher b values of Co_1Ga_1-LDH/MXene compared to $Co_1Ga_{0.5}$-LDH/MXene demonstrate greater capacitive contribution, suggesting faster charge storage/release kinetics. To further distinguish the relative contributions of diffusion and capacitance, a modified power law is employed:

$$i = k_1 \times v + k_2 \times v^{1/2} \tag{9}$$

where v is the scan rate, i is the output (current density), and k_1 and k_2 are the capacitive and diffusive coefficients, respectively. The linear relationship between v and the coefficient k_1 reflects double-layer formation and surface adsorption processes. In contrast, the semi-infinite diffusion governed faradaic processes exhibit $v^{1/2}$ dependence via parameter k_2. Fig. 5g shows the ratios of diffusion to capacitance contributions for Co_1Ga_0-LDH/MXene, $Co_1Ga_{0.5}$-LDH/MXene, and Co_1Ga_1-LDH/MXene at different scan rates. The capacitive contributions increase with scan rates, indicating enhanced dominance of surface capacitance effects at higher scan rates. This trend arises from optimized charge transfer kinetics and reduced ion migration distances, which promote surface charge storage. Fig. 5h shows the capacitances of the Co_1Ga_1-LDH/MXene composite electrode at scan rates of 10–50 mV/s. The material exhibits excellent capacitive properties, with contributions increasing from 34.79 % (10 mV/s) to 86.16 % (50 mV/s), indicating a significant shift toward capacitance dominance at higher scan rates. These findings suggest that the electrochemical behavior of the electrode involves combined diffusion-controlled and capacitance-controlled processes.

The Warburg impedance of MXene is analyzed using EIS data and Nyquist plots in the frequency range of 0.01 Hz to 1 MHz. The equivalent circuit model is constructed using the *Z*-view software to fit the impedance data. As shown in Fig. 6a, Co_1Ga_1-LDH/MXene exhibits the largest slope and lowest impedance, implying that electrolyte ions can penetrate the electrode more efficiently. Fig. 6a (inset) shows a magnified view of the high-frequency region for clearer interpretation of the charge transfer resistance (R_{ct}) and internal resistance (R_s), with corresponding values listed in Fig. 6b. The R_s values are: Co-LDH (2.92 Ω), MXene (2.20 Ω), Co_1Ga_0-LDH/MXene (2.07 Ω), $Co_1Ga_{0.5}$-LDH/MXene (2.24 Ω), and Co_1Ga_1-LDH/MXene (0.88 Ω). R_s primarily reflects the contact resistance at the electrolyte-electrode interface, the ion resistance in the electrolyte, and the intrinsic resistance of the current collector. Notably, Co_1Ga_1-LDH/MXene demonstrates the lowest R_s and R_{ct} (3.763 Ω).

The cycling stability is a critical performance metric for electrode materials. As shown in Fig. 6e, the capacitance retention rates of the three electrodes are measured after 6000 cycles at 5 A/g. Co_1Ga_1-LDH/MXene delivers the best stability by retaining 85.13 % of its initial capacitance. The EIS curve in Fig. 6c, reveal minimal changes for Co_1Ga_1-LDH/MXene after cycling, with corresponding R_s and R_{ct} increments of 0.53 Ω and 1.11 Ω (quantified in Fig. 6d), respectively. The small resistance increases indicate that the electrode maintains good structural integrity and electrochemical stability during cycling, suggesting promising potential for long-term practical applications.

An ASC device was assembled using Co_1Ga_1-LDH/MXene as the cathode, AC as the anode, and 7 M KOH as the electrolyte. Unlike symmetric supercapacitors (SSc) assembled with identical electrode materials, this asymmetric design synergizes the faradaic energy storage of the anode with the electric double-layer capacitance of the cathode, enabling an extended voltage window and enhanced energy density. Fig. 7a shows the ASC structure (Co_1Ga_1-LDH/MXene//AC) and the ion migration during charging and discharging. The hydroxyl groups on the surface of MXene adsorb metal ions from LDH, facilitating rapid electron transfer. The CV curves in, Fig. 7b show a good match between the Co_1Ga_1-LDH/MXene cathode (0–0.6 V) and AC anode (−1 to 0 V) at 20 mV/s, supported by complementary GCD/CV data for AC in Fig. S5. To determine the optimal voltage window, the CV and GCD curves of the ASC are analyzed across different voltage windows (Fig. 7f and g). Theoretical predictions indicate an ideal operating window of 0 to 1.6 V. Fig. 7c presents the CV curves at scan rates from 1 to 50 mV/s, confirming the electrochemical stability of the ASC.

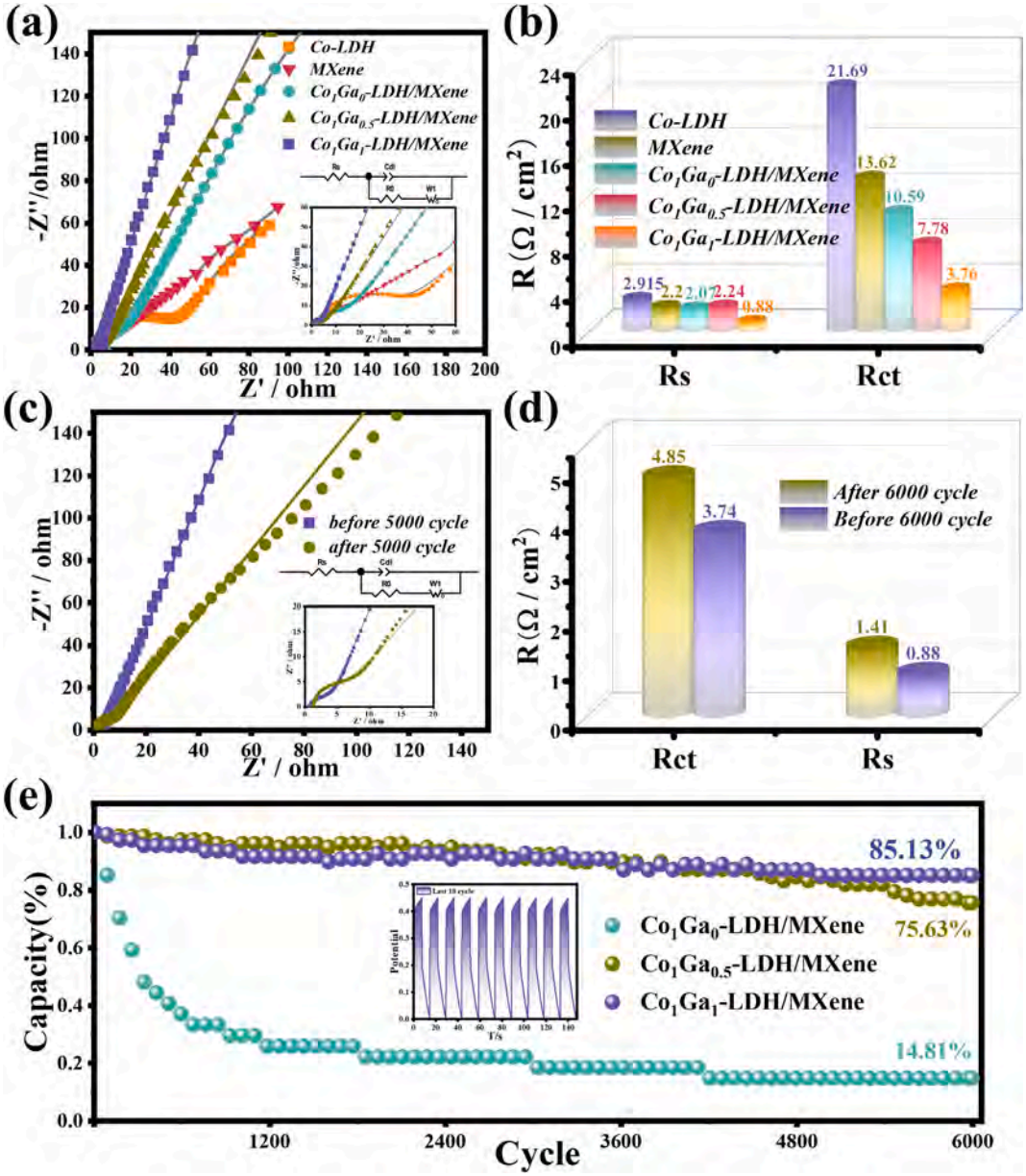

Fig. 6. (a) Nyquist plots and equivalent circuits and (b) R_s and R_{ct} values for Co-LDH, MXene, Co_1Ga_0-LDH/MXene, $Co_1Ga_{0.5}$-LDH/MXene and Co_1Ga_1-LDH/MXene; (c) EIS spectra before and after 6000 cycles and (d) R_s and R_{ct} values of Co_1Ga_1-LDH/MXene before and after 6000 cycles; (e) 6000-cycle stability test for Co_1Ga_0-LDH/MXene, $Co_1Ga_{0.5}$-LDH/MXene and Co_1Ga_1-LDH/MXene at 5 A/g.

Fig. 7d shows the GCD curves of the ASC at different current density, while Fig. 7e shows the variations in the specific capacitance and Coulombic efficiency with different current densities. The ASC device achieves a maximum specific capacitance of 364.40 F/g at 0.25 A/g, retaining 247.80 F/g at 1.5 A/g (68.01 % retention). Kinetic analysis confirms that the primary energy storage mechanism in the Co_1Ga_1-LDH/MXene//AC hybrid device is surface-controlled capacitance, evidenced by the broad peaks and high *b* values in Fig. 7h.

To further explore the role of diffusion and capacitive processes in energy storage, Fig. 8a and b shows that the capacitive contribution ratio increases from 16.25 % (5 mV/s) to 58.28 % (40 mV/s). This trend indicates enhanced capacitive-dominated storage at higher scan rates, as diffusion processes become kinetically limited. Fig. 8c shows the long-term cycling stability of the Co_1Ga_1-LDH/MXene//AC device at 9 A/g for 6000 cycles, showing 81.24 % capacitance retention (purple line) and 99.2 % Coulombic efficiency (blue line). EIS measurements before and after cycling confirm the stability during long-term cycling. Fig. 8d presents the Nyquist plots of the Co_1Ga_1-LDH/MXene//AC device before and after cycling, with the inset showing the corresponding equivalent circuit. Notably, the charge transfer resistance reaches a minimum of 3.56 Ω during the charging-discharging process. The Nyquist diagram exhibits negligible changes after cycling, with R_s and R_{ct} increasing by only 1.54 Ω and 7.07 Ω, respectively, reflecting minimal structural change and degradation.

The Co_1Ga_1-LDH/MXene//AC device delivers exceptional energy storage performance, achieving a peak energy density of 91.73 Wh/kg at 375 W/kg (Fig. 8e). Even at a higher power density of 1125 W/kg, the energy density remains at 77.44 Wh/kg. Compared to previously reported SCs based on LDHs [54], this ASC exhibits significantly higher power and energy densities. Co-MXene@NF//PANI@CFP shows an energy density of 26.06 Wh/kg at a power density of 700 W/kg, while 300-CoS@MXene/CF-31:1//AC shows 10.66 Wh/kg at 135.96 W/kg. NiCo$_2$O$_4$@rGO/ACF//$Ti_3C_2T_x$/ACF shows 44.36 Wh/kg at 985 W/kg, and NiCoFe-LDH/Ti_3C_2//rGO attains 54.4 Wh/kg at 895.1 W/kg.

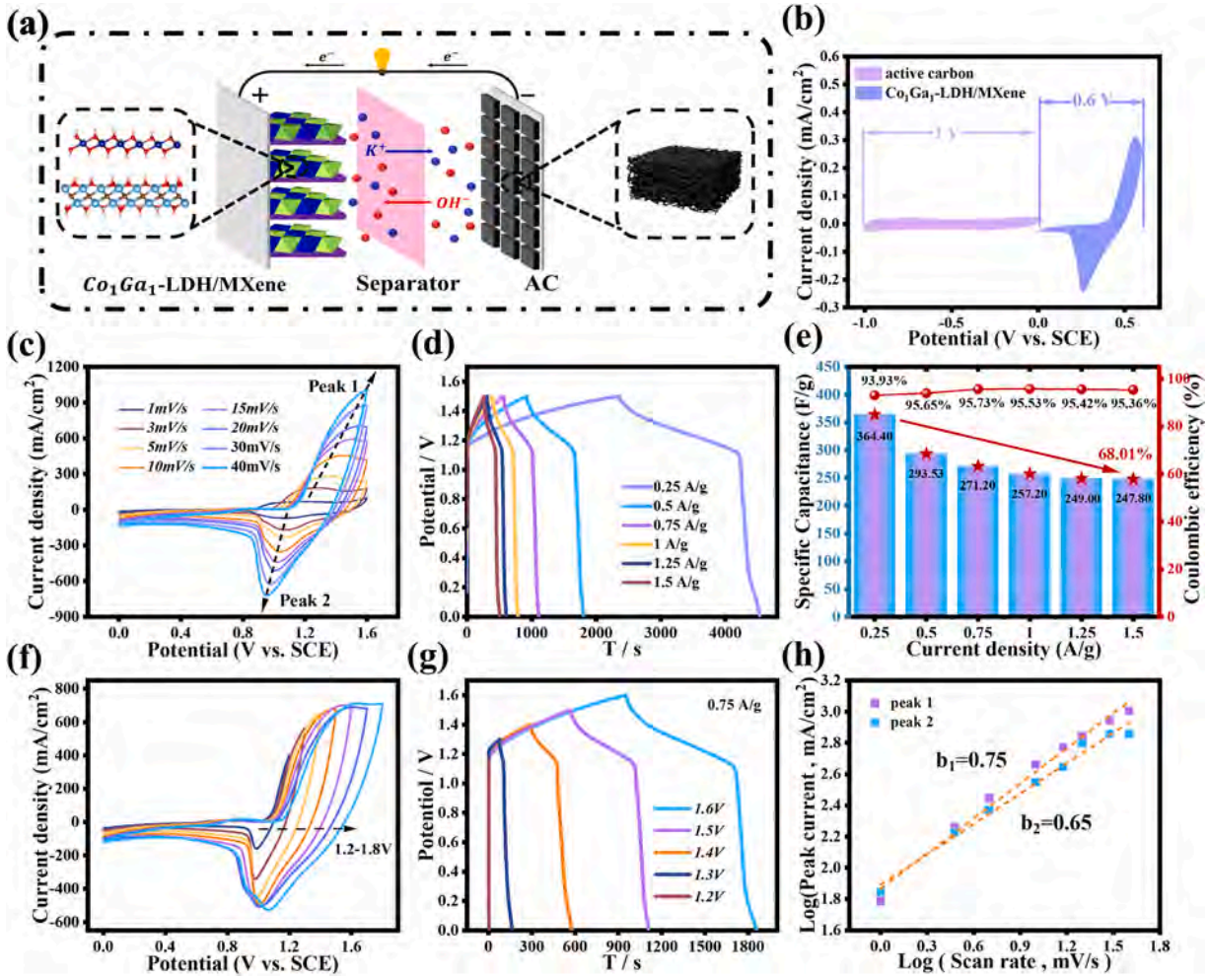

Fig. 7. Co_1Ga_1-LDH/MXene//AC device: (a) ACS schematic; (b) CV curves of Co_1Ga_1-LDH/MXene with AC electrodes; (c) CV curves at different scanning rates; (d) GCD curves at different current densities; (e) Specific capacitance and Coulombic efficiency for different current densities; (f) CV curves for several voltage ranges; (g) GCD curves for several voltage ranges; (h) Determination of *b* values of the anodic and cathodic peaks.

Additionally, MXene/CoS_2//rGO maintains 28.8 Wh/kg at 800 W/kg, while AC/$NiCo_2S_4$//AC achieves 23.3 Wh/kg at 335.8 W/kg. The MXene/CoAl-LDH//MXene/graphene combination has superior characteristics, such as 30.9 Wh/kg at 992.6 W/kg, and $NiCo_2S_4$@$NiCo_2S_4$//rGO reaches 32 Wh/kg even at 375 W/kg. The comprehensive comparison underscores the exceptional characteristics of our ASC. To rigorously assess the storage capacity of the ASC, a 20-s charge at 2.8 V enables the device to deliver exceptional burst power—sustaining a 3 V DC micro-fan for 70 s and powering a small timer for 86 s. This performance not only surpasses conventional capacitors but also highlights its potential for high-demand burst-power applications, such as emergency lighting and sensor networks, where rapid energy discharge is critical.

4. Conclusion

This work demonstrates a rational design strategy to synergistically integrate bimetallic CoGa-LDH with $Ti_3C_2T_x$ MXene, overcoming the inherent challenges of MXene restacking and limited active-site exposure in LDHs. Optimizing the Co/Ga atomic ratio enables structural refinement, where self-assembly suppresses MXene restacking and generates oxygen vacancies via competitive coordination between metastable metal ions and surface hydroxyl groups. The vacancies dynamically reconfigure the electronic environment to enhance the charge transfer kinetics and create abundant redox-active interfaces. The Co_1Ga_1-LDH/MXene composite delivers exceptional single-electrode performance, achieving a high specific capacitance of 1345.3 F/g at 1 A/g and 94.45 % Coulombic efficiency, significantly outperforming the Ga-deficient counterparts (Co_1Ga_0-LDH/MXene: 162.6 F/g; $Co_1Ga_{0.5}$-LDH/MXene: 644 F/g). DFT calculations reveal that Ga^{3+} incorporation modulates the electronic structure by shifting the Co *d*-band center from −1.84 eV to −1.67 eV and optimizing the K^+ adsorption energy to −2.36 eV to collectively enhance the redox activity and ion diffusion. To demonstrate the commercial feasibility, the ASC device shows a high energy density (77.44 Wh/kg) at a power density (1125 W/kg) as well as excellent cycling stability. This study reveals a promising approach to overcome the technical challenges that have hampered the development of high-performance SCs.

CRediT authorship contribution statement

Chenxi Li: Writing – review & editing, Writing – original draft, Visualization, Validation, Software, Methodology, Investigation, Data curation, Conceptualization. **Mai Li:** Writing – review & editing, Validation, Supervision, Resources, Project administration, Funding acquisition, Conceptualization. **Xiang Peng:** Validation, Resources, Data curation. **Inaam Ullah:** Validation, Investigation, Formal analysis, Conceptualization. **Haotian Hu:** Visualization, Investigation, Formal analysis. **Jiayi Shen:** Investigation, Data curation, Conceptualization. **Ayesha Irfan:** Visualization, Investigation, Formal analysis, Data

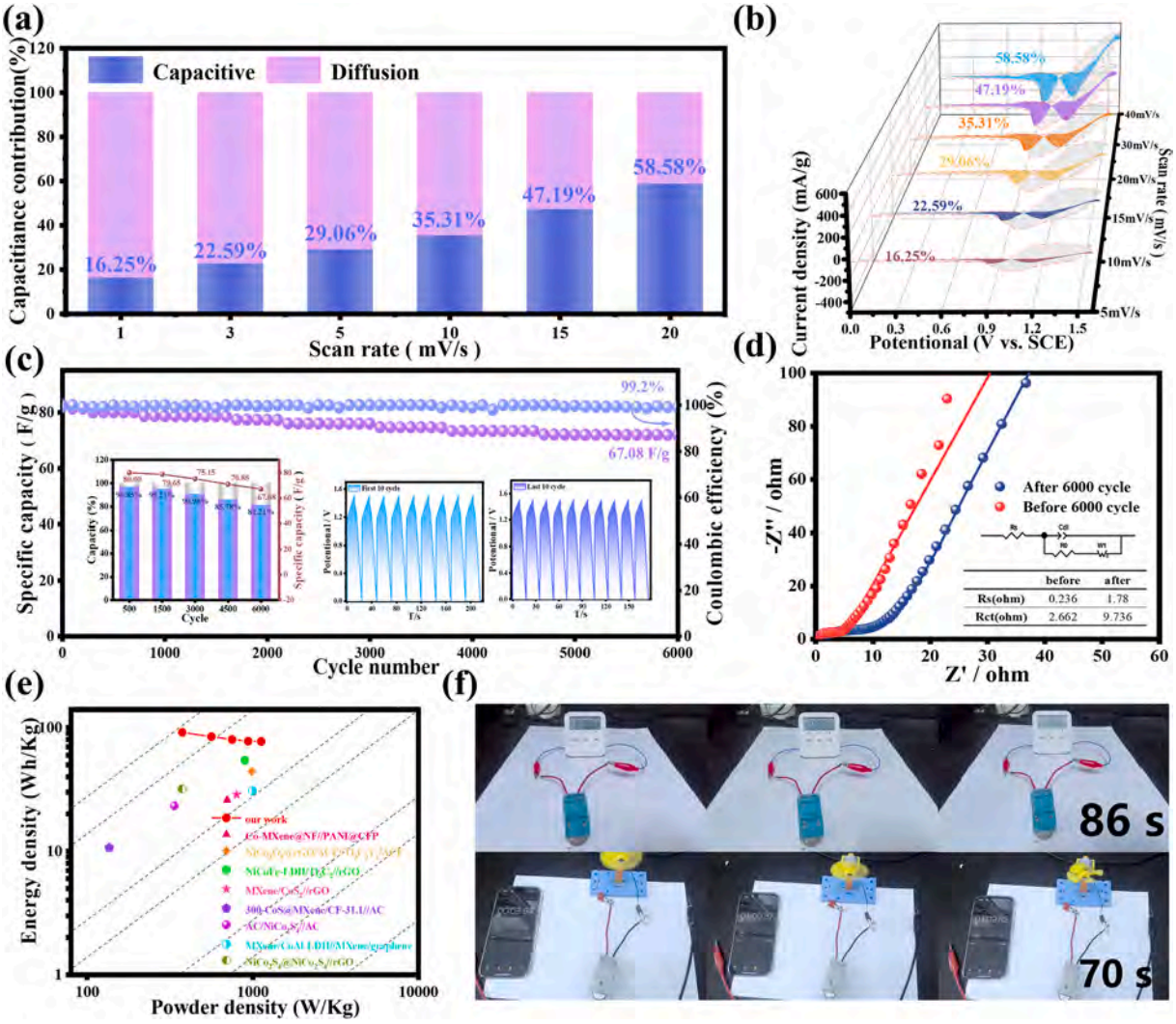

Fig. 8. Co_1Ga_1-LDH/MXene//AC device: (a) Capacitive contribution to the total current at different scanning rates; (b) Capacitive contribution ratios at different scanning rates; (c) Retention and Coulombic efficiency of the ASC; (d) EIS before and after 6000 cycles; (e) Ragone plots; (f) ASC powering a digital timer and a micro-fan.

curation. **Wendong Xu:** Investigation. **Paul K. Chu:** Writing – review & editing, Visualization, Funding acquisition.

Declaration of competing interest

The authors declare that they have no known competing financial interests or personal relationships that could have appeared to influence the work reported in this paper.

Acknowledgments

This research was supported by the Fundamental Research Funds for the Central Universities (No. 2232024D-31), the National Natural Science Foundation of China (No. 22005046), and the Natural Science Foundation of Shanghai (No. 21ZR1402900), the Fundamental Research Funds for the Central Universities (No. 202410255080).

Appendix A. Supplementary data

Supplementary data to this article can be found online at https://doi.org/10.1016/j.jcis.2025.138240.

Data availability

Data will be made available on request.

References

[1] Z. Guo, X. Han, C. Zhang, S. He, K. Liu, J. Hu, W. Yang, S. Jian, S. Jiang, G. Duan, Activation of biomass-derived porous carbon for supercapacitors: a review, Chin. Chem. Lett. 35 (7) (2024) 109007.
[2] W.H. Zhu, B.J. Tatarchuk, Characterization of asymmetric ultracapacitors as hybrid pulse power devices for efficient energy storage and power delivery applications, Appl. Energy 169 (2016) 460–468.
[3] Y. Xu, Y. Du, H. Chen, J. Chen, T. Ding, D. Sun, D.H. Kim, Z. Lin, X. Zhou, Recent advances in rational design for high-performance potassium-ion batteries, Chem. Soc. Rev. 53 (13) (2024) 7202–7298.
[4] P.S. Dighe, R.S. Redekar, N.L. Tarwal, P.B. Sarawade, Design and development of the high-performance aqueous asymmetric supercapacitor based on the hydrothermally grown binder-less Ni-co LDH nanosheets, J. Energy Storage 88 (2024) 111467.
[5] S.N. Kanimozhi, A. Kadangodan Putiyaveettil, B. Natesan, A. Al Souwaileh, J. J. Wu, G. Landi, A. Sambandam, Design of co–Al–Mn LDH@Ti_2CT_x asymmetric supercapacitor: a comprehensive study on the role of redox electrolyte and its application in flexible electronics, ACS Appl. Electron. Mater. 6 (2) (2024) 918–930.
[6] L.I. Schultz, N.P. Querques, Tracing the ultracapacitor commercialization pathway, Renew. Sust. Energ. Rev. 39 (2014) 1119–1126.

[7] L.C. Meyer, A.K. Thiagarajan, A. Koposov, A. Balducci, Unravelling the mechanism of potassium-ion storage into graphite through electrolyte engineering, Energy Storage Mater. 75 (2025) 104021.

[8] F. Xiao, J. Zhang, W. Zhou, Y. Fang, X. He, W. Lai, C. Lin, M. Ge, H. Fan, Q. Qian, M. Wei, Q. Chen, L. Zeng, Defect-engineered WS_xSe_{2-x} nanocrystals anchored on selenized polyacrylonitrile fibers toward high-performance sodium/potassium-ion batteries with a wide working temperature range, Inorg. Chem. Front. 11 (7) (2024) 2164–2177.

[9] Y. Wang, F. Zhang, Q. Long, S. Li, D. Guo, Z. Zhu, H. Zhang, Enhancing cyclic stability of Mn-based Prussian blue cathode for potassium ion storage by high-spin Fe substitution strategy, Energy Storage Mater. 71 (2024) 103399.

[10] P. Zhang, Y. Wei, S. Zhou, R.A. Soomro, M. Jiang, B. Xu, A metal-organic framework derived approach to fabricate in-situ carbon encapsulated bi/Bi_2O_3 heterostructures as high-performance anodes for potassium ion batteries, J. Colloid Interface Sci. 630 (2023) 365–374.

[11] G. Lee, K. Kim, E. Lim, J. Hwang, Scalable Ambient Synthesis of Metal–Organic Frameworks and Their Derivative Nanoporous Carbon for Superior Potassium Ion Storage, ACS Sustain. Chem. Eng. 12 (39) (2024) 14524–14533.

[12] Q. Zhang, J. Mao, W.K. Pang, T. Zheng, V. Sencadas, Y. Chen, Y. Liu, Z. Guo, Boosting the potassium storage performance of alloy-based anode materials via electrolyte salt chemistry, Adv. Energy Mater. 8 (15) (2018) 1703288.

[13] J. Xu, S. Dou, X. Cui, W. Liu, Z. Zhang, Y. Deng, W. Hu, Y. Chen, Potassium-based electrochemical energy storage devices: development status and future prospect, Energy Storage Mater. 34 (2021) 85–106.

[14] X. Wei, B. Liu, Z. Chen, K. Wu, Y. Liu, X. Yuan, X. Zhang, X. Liu, Q. Wan, Y. Song, Recent advances in modulation engineering-enabled metal compounds for potassium-ion storage, Energy Storage Mater. 51 (2022) 815–839.

[15] W. Zhang, R. Huang, X. Yan, C. Tian, Y. Xiao, Z. Lin, L. Dai, Z. Guo, L. Chai, Carbon electrode materials for advanced potassium-ion storage, Angew. Chem. Int. Ed. 62 (43) (2023) e202308891.

[16] H. Zhang, Y. Bai, H. Chen, J. Wu, C.M. Li, X. Su, L. Zhang, Oxygen-defect-rich 3D porous cobalt-gallium layered double hydroxide for high-performance supercapacitor application, J. Colloid Interface Sci. 608 (2022) 1837–1845.

[17] S. Asaithambi, P. Sakthivel, M. Karuppaiah, R. Yuvakkumar, D. Velauthapillai, T. Ahamad, M.A.M. Khan, M.K.A. Mohammed, N. Vijayaprabhu, G. Ravi, The bifunctional performance analysis of synthesized Ce doped SnO_2/g-C_3N_4 composites for asymmetric supercapacitor and visible light photocatalytic applications, J. Alloys Compd. 866 (2021) 158807.

[18] W. Xu, M. Li, W.U. Hasan, Z. Meng, H. Hu, I. Ullah, A. Irfan, J. Shen, P.K. Chu, Composition-optimized NiGa-LDH on MOF-derived and cobalt-nanoparticles-embedded carbon flakes for enhanced potassium-ion storage, Chem. Eng. J. 499 (2024) 155931.

[19] I. Ullah, J. Jacob, F.F. Al-Harbi, K. Mahmood, A. Ali, M. Tamseel, S. Ikram, N. Amin, K. Javaid, L. Ben Farhat, S. Hussain, M. Yasir Ali, Investigating the potential of AgZnO thin film composites for waste heat recovery using Seebeck data, Opt. Mater. 127 (2022) 112318.

[20] B. Shen, X. Hu, H.-T. Ren, H.-K. Peng, B.-C. Shiu, J.-H. Lin, C.-W. Lou, T.-T. Li, Rosette-like (Ni,Co)Se_2@Nb_2CT_x MXene heterostructure with abundant Se vacancies for high-performance flexible supercapacitor electrodes, Chem. Eng. J. 484 (2024) 149440.

[21] R. Shivani, A.K. Duddi, N. Singh, S. Kamboj, Kumar, enhancing the performance of Zn-ion capacitors with electrochemically tailored NiCo-LDH@Co_3O_4 nanoflakes on Ni foam, J. Energy Storage 91 (2024) 112028.

[22] P. Sakthivel, G. Anandha Babu, M. Karuppiah, S. Asaithambi, V. Balaji, M. S. Pandian, P. Ramasamy, M.K.A. Mohammed, N. Navaneethan, G. Ravi, Electrochemical energy storage applications of carbon nanotube supported heterogeneous metal sulfide electrodes, Ceram. Int. 48 (5) (2022) 6157–6165.

[23] Q. Yang, K. Lv, L. Liang, J. Ma, C. Liu, X. Yan, M. Wang, H. Yao, D. Wei, D. Ma, K. Xie, Layered double hydroxides as high-performance anode material for potassium ion battery, J. Alloys Compd. 882 (2021) 160711.

[24] S. Yang, Z. Xu, J. Xu, J. Lu, D. Zhang, S. Ni, High capacity Li_3VO_4-Ga_2O_3/NC as durable anode for Li-ion batteries via robust pseudocapacitive charge storage, J. Alloys Compd. 868 (2021) 159115.

[25] Z.-H. He, J.-F. Gao, L.-B. Kong, Iron gallium oxide with high-capacity and super-rate performance as new anode materials for Li-ion capacitors, Energy Fuel 35 (9) (2021) 8378–8386.

[26] X. Chen, H. Chai, Y. Cao, W. Zhou, Y. Li, Y. Yang, Hierarchical CoGa layered double hydroxides grown on nickel foam as high energy density hybrid supercapacitor, Chem. Eng. J. 381 (2020) 122620.

[27] S. Liu, K.S. Hui, K.N. Hui, H.-F. Li, K.W. Ng, J. Xu, Z. Tang, S.C. Jun, An asymmetric supercapacitor with excellent cycling performance realized by hierarchical porous $NiGa_2O_4$ nanosheets, J. Mater. Chem. A 5 (36) (2017) 19046–19053.

[28] J. Li, S. Li, Y. Huang, Z. Liu, C. Chen, Q. Ding, H. Xie, Y. Xu, S. Sun, H. Li, Constructing Hierarchical $CoGa_2O_4$–S@NiCo-LDH Core–Shell Heterostructures with Crystalline/Amorphous/Crystalline Heterointerfaces for Flexible Asymmetric Supercapacitors, ACS Appl. Mater. Interfaces 16 (6) (2024) 6998–7013.

[29] J. Li, J.-F. Gao, Z.-H. He, J.-F. Hou, L.-B. Kong, Nanoflower architecture $NiGa_2O_4$ with a spinel structure modified by 2D layered RGO for enhanced Li-ion battery anode performance, Energy Fuel 36 (4) (2022) 2149–2158.

[30] M.C. Freitas, A.L. Sanati, P.A. Lopes, A.F. Silva, M. Tavakoli, 3D printed gallium battery with outstanding energy storage: toward fully printed battery-on-the-board soft electronics, Small 20 (20) (2024) 2304716.

[31] A. Irfan, I. Ullah, M. Li, W. Xu, Z. Dong, H. Zhao, H. Hu, N. Irshad, K. Yang, P. Zhong, P.K. Chu, Synergistic effects of hybrid CuS@$Ti_3C_2T_x$/MXene material for enhanced super capacitive energy storage and efficient water splitting, Surfaces and Interfaces 56 (2025) 105536.

[32] M. Naguib, V.N. Mochalin, M.W. Barsoum, Y. Gogotsi, 25th anniversary article: MXenes: a new family of two-dimensional materials, Adv. Mater. 26 (7) (2014) 992–1005.

[33] S. Gohri, J. Madan, D.P. Samajdar, S. Bhattarai, M.K.A. Mohammed, M. Khalid Hossain, M. Ferdous Rahman, A.K. Al-Mousoi, E.A. Al-Ammar, R. Pandey, Achieving 24.6% efficiency in 2D perovskite solar cells: Bandgap tuning and MXene contact optimization in (BDA)$(MA)_{n-1}Pb_nI_{3n+1}$ structures, Chem. Phys. Lett. 845 (2024) 141291.

[34] I. Ullah, A. Irfan, M. Li, S. Saddique, T. Yang, H. Zhao, N. Irshad, K. Yang, C. Wang, P.K. Chu, Optimizing ZnSe microspheres through 2D MXene for asymmetric pseudocapacitive supercapacitors and efficient hydrogen production via water splitting, J. Power Sources 643 (2025) 237046.

[35] R. Zhao, M. Wang, D. Zhao, H. Li, C. Wang, L. Yin, Molecular-level Heterostructures assembled from titanium carbide MXene and Ni–co–Al layered double-hydroxide Nanosheets for all-solid-state flexible asymmetric high-energy supercapacitors, ACS Energy Lett. 3 (1) (2018) 132–140.

[36] G. Anandha Babu, S. Perumal, M.K.A. Mohammed, M. Govindasamy, A. A. Alothman, M. Ouladsmane, R. Ganesan, An ultra-high electrochemical performance of surface-rich boron induced multi-metal centered heterocatalyst for overall water splitting, Int. J. Hydrog. Energy 54 (2024) 652–664.

[37] R. Zhang, J. Dong, W. Zhang, L. Ma, Z. Jiang, J. Wang, Y. Huang, Synergistically coupling of 3D FeNi-LDH arrays with $Ti_3C_2T_x$-MXene nanosheets toward superior symmetric supercapacitor, Nano Energy 91 (2022) 106633.

[38] H. Hu, M. Li, W. Xu, C. Li, A. Irfan, I. Ullah, W. Ul Hasan, Q. Deng, Z. Meng, J. He, Z. Sun, X. Peng, CdSe nanoparticles synergized with 2D $Ti_3C_2T_x$ MXene as the dual-function composite for enhanced K^+ ion storage and water splitting, ACS Appl. Mater. Interfaces 17 (16) (2025) 23834–23847.

[39] M.Z. Nawaz, A. Khaleeq, W.U. Hasan, W. Ahmad, R.Z.A. Manj, M.S. Saleem, I. Ullah, A. Irfan, I.M. Ul Hasan, M. Yaqub, H.M.N.U.H.K. Asghar, G. Naz, M. Li, C. Wang, Y.Y. Illarionov, Flexible self-powered $Ti_3C_2T_x$ MXene Nanosheet/CdS Nanobelt photodetector with enhanced responsivity and photosensitivity, ACS Appl. Nano Mater. 8 (21) (2025) 11015–11025.

[40] I. Ullah, M. Tamseel, M. Amami, M.R. Javed, K. Javaid, K. Mahmood, S. Ikram, A. Ali, N. Amin, M.S. Hussain, M.Y. Ali, M.I. Arshad, Growth and characterization of ag–Al_2O_3 composites thin films for thermoelectric power generation applications, Ceram. Int. 48 (3) (2022) 3647–3651.

[41] J. Li, X. Ge, Q. Liang, Z. Wang, W. Han, X. Zhou, M. Lu, W. Zhang, W. Zheng, Quantitative pre-intercalation of alkali metal ions enables precisely modulating Li + storage of MXenes, Energy Storage Mater. 73 (2024) 103828.

[42] Y. Xue, S. Chao, M. Xu, Q. Wu, Q. Zhang, Y.-J. Liu, F. Wu, L. Liu, M.S. Javed, W. Zhang, Multi-layers hexagonal hole MXene trap constructed by carbon vacancy defect regulation strategy enables high energy density potassium-ions storage, Energy Storage Mater. 71 (2024) 103558.

[43] C. Li, Z. Dai, W. Liu, P. Kantichaimongkol, P. Yu, P. Pattananuwat, J. Qin, X. Zhang, A self-sacrifice template strategy to synthesize co-LDH/MXene for lithium-ion batteries, Chem. Commun. 57 (86) (2021) 11378–11381.

[44] H. Qiu, X. Sun, S. An, D. Lan, J. Cui, Y. Zhang, W. He, Microwave synthesis of histidine-functionalized graphene quantum dots/Ni-co LDH with flower ball structure for supercapacitor, J. Colloid Interface Sci. 567 (2020) 264–273.

[45] Y. Wu, H. Zhao, P. Huang, Y. Zhang, R. Deng, Y. Xu, CoGa-layered double hydroxides modified tin-doped hematite photoanode for efficient solar water splitting, Chem. Eng. Sci. 302 (2025) 120850.

[46] J. Xu, X. Zhong, X. Wu, Y. Wang, S. Feng, Optimizing the electronic spin state and delocalized electron of $NiCo_2(OH)_x$/MXene composite by interface engineering and plasma boosting oxygen evolution reaction, J. Energy Chem. 71 (2022) 129–140.

[47] L. Pu, J. Zhang, N.K.L. Jiresse, Y. Gao, H. Zhou, N. Naik, P. Gao, Z. Guo, N-doped MXene derived from chitosan for the highly effective electrochemical properties as supercapacitor, Adv. Compos. Hybrid Mater. 5 (1) (2022) 356–369.

[48] M. Shi, M. Narayanasamy, C. Yang, L. Zhao, J. Jiang, S. Angaiah, C. Yan, 3D interpenetrating assembly of partially oxidized MXene confined Mn–Fe bimetallic oxide for superior energy storage in ionic liquid, Electrochim. Acta 334 (2020) 135546.

[49] J. Halim, K.M. Cook, M. Naguib, P. Eklund, Y. Gogotsi, J. Rosen, M.W. Barsoum, X-ray photoelectron spectroscopy of select multi-layered transition metal carbides (MXenes), Appl. Surf. Sci. 362 (2016) 406–417.

[50] C. Zhu, C. Pei, H.S. Park, X. Yu, Design of 2D/2D heterostructure by coupling cobalt hydroxides with Mxene on nickel foam for high energy density supercapacitors, J. Alloys Compd. 948 (2023) 169809.

[51] Y. Liang, H. Shen, J. Li, H. Zhao, J. Xu, H. Huang, S. Xu, X. Liang, W. Zhou, J. Guo, Tailoring surface terminals of $Ti_3C_2T_x$ MXene microgels via interlayer domain-confined polyphosphate ammonium for flexible supercapacitor applications, Chem. Eng. J. 497 (2024) 154775.

[52] Z. Cai, Y.-F. Ma, M. Wang, A.N. Qian, Z.-M. Tong, L.-T. Xiao, S.-T. Jia, X.-Y. Chen, Engineering of electrolyte ion channels in MXene/holey graphene electrodes for superior supercapacitive performances, Rare Metals 41 (6) (2022) 2084–2093.

[53] C. Jing, S. Tao, B. Fu, L. Yao, F. Ling, X. Hu, Y. Zhang, Layered double hydroxide-based nanomaterials for supercapacitors and batteries: strategies and mechanisms, Prog. Mater. Sci. 150 (2025) 101410.

[54] S. Alam, F. Fiaz, M.I. Khan, M.Z. Iqbal, Z. Ahmad, H.H. Hegazy, Recent advancements in the performance of MXene and its various composites as an electrode material in asymmetric supercapacitors, J. Alloys Compd. 961 (2023) 171007.

Supporting Information

Interlayer-Engineered MXene Nanosheets Confining CoGa-LDH Enable Ultrafast Charge Transfer Kinetics for High-Energy Potassium-Ion Supercapacitors

Chenxi Li[a], Mai Li[a*], Xiang Peng[b], Inaam Ullah[a], Haotian Hu[a], Jiayi Shen[a], Ayesha Irfan[a], Wendong Xu[a], and Paul K. Chu[c]

[a] College of Physics, Donghua University, Shanghai 201620, China

[b] Hubei Key Laboratory of Plasma Chemistry and Advanced Materials, Engineering Research Center of Phosphorus Resources Development and Utilization of Ministry of Education, School of Materials Science and Engineering, Wuhan Institute of Technology, Wuhan 430205, China

[c] Department of Physics, Department of Materials Science and Engineering, and Department of Biomedical Engineering, City University of Hong Kong, Tat Chee Avenue, Kowloon, Hong Kong, China

* Corresponding authors: E-mail: limai@dhu.edu.cn (M. Li)

1. Materials characterization

The crystal structure of the samples was analyzed using X-ray diffraction (XRD, D/max trr-iii, Cu Kα). The morphology and elemental distribution were characterized by scanning electron microscopy (SEM, SUPRA 40, Zeiss, Germany) and transmission electron microscopy (TEM, JEM-2100F) at 5 kV and 200 kV, respectively. X-ray photoelectron spectroscopy (XPS) was performed on the Thermo Escalab 250Xi to determine the chemical states and composition of the samples. Raman scattering was conducted at room temperature on the Renishaw inVia Raman microscope equipped with a 532 nm solid-state laser.

2. Electrochemical evaluation

The electrochemical tests, including cyclic voltammetry (CV), constant-current charge/discharge (GCD), and electrochemical impedance spectroscopy (EIS), were conducted on a CH Instruments Model 660E workstation (CH Instruments, Inc., USA) at room temperature. In the three-electrode configuration, the nickel foam loaded with the active materials was the working electrode (WE), a mercury glycol electrode (SCE) was the reference electrode, and graphite flakes served as the counter electrode. The ASC with a two-electrode configuration employed Co_1Ga_1-LDH/MXene as the positive electrode and activated carbon (AC) as the negative electrode. Both electrodes were cut into 12 mm diameter discs, and uniform mass loading and geometric alignment were ensured. The device was packaged in a CR2032 coin cell with 7 M KOH as the electrolyte and an NKK-MPF30AC-100 separator to prevent electrical shorting.

The equations for specific capacitance (C, F/g), power density (P, W/kg), and energy density (E, Wh/kg) are as follows:

$$C = I\Delta t/m\Delta V \quad (1)$$

$$P = 3600E/\Delta t \quad (2)$$

$$E = C(\Delta V)^2/2 \times 3.6 \quad (3)$$

I (A) is the discharge current, Δt is the discharge time t (s), m (g) is the mass loading of the electrode, ΔV (V) is the discharge voltage window, and C (F/g) is the specific capacitance of the cathode material.

3. Theoretical evaluation

First-principles calculations were performed using spin-polarized density functional theory (DFT) within the generalized gradient approximation (GGA) employing the Perdew-Burke-Ernzerhof (PBE) functional. The projector augmented wave (PAW) method was used to describe ionic cores, while valence electrons were expanded in a plane-wave basis set with a kinetic energy cutoff of 450 eV. Partial occupancies of the Kohn-Sham orbitals were treated by Gaussian smearing using a width of 0.1 eV. Electronic convergence was achieved when the energy difference between successive steps fell below 10-5 eV, and geometric optimization was considered complete when the maximum force on any atom was less than 0.02 eV/Å. To account for dispersion interactions, Grimme's DFT-D3 correction was applied. The adsorption energy (E_{ads}) of K was defined as:

$$E_{ads} = E_{K/surf} - E_{surf} - E_{K(g)}, \quad (1)$$

where $E_{K/surf}$ indicates K adsorbate energy, E_{surf} represents pristine surface energy, and $E_{K(g)}$ is the isolated K molecule energy in a 20 Å cubic periodic box. The 1x1x1 Monkhorst-Pack k-point grid was used in Brillouin zone sampling.

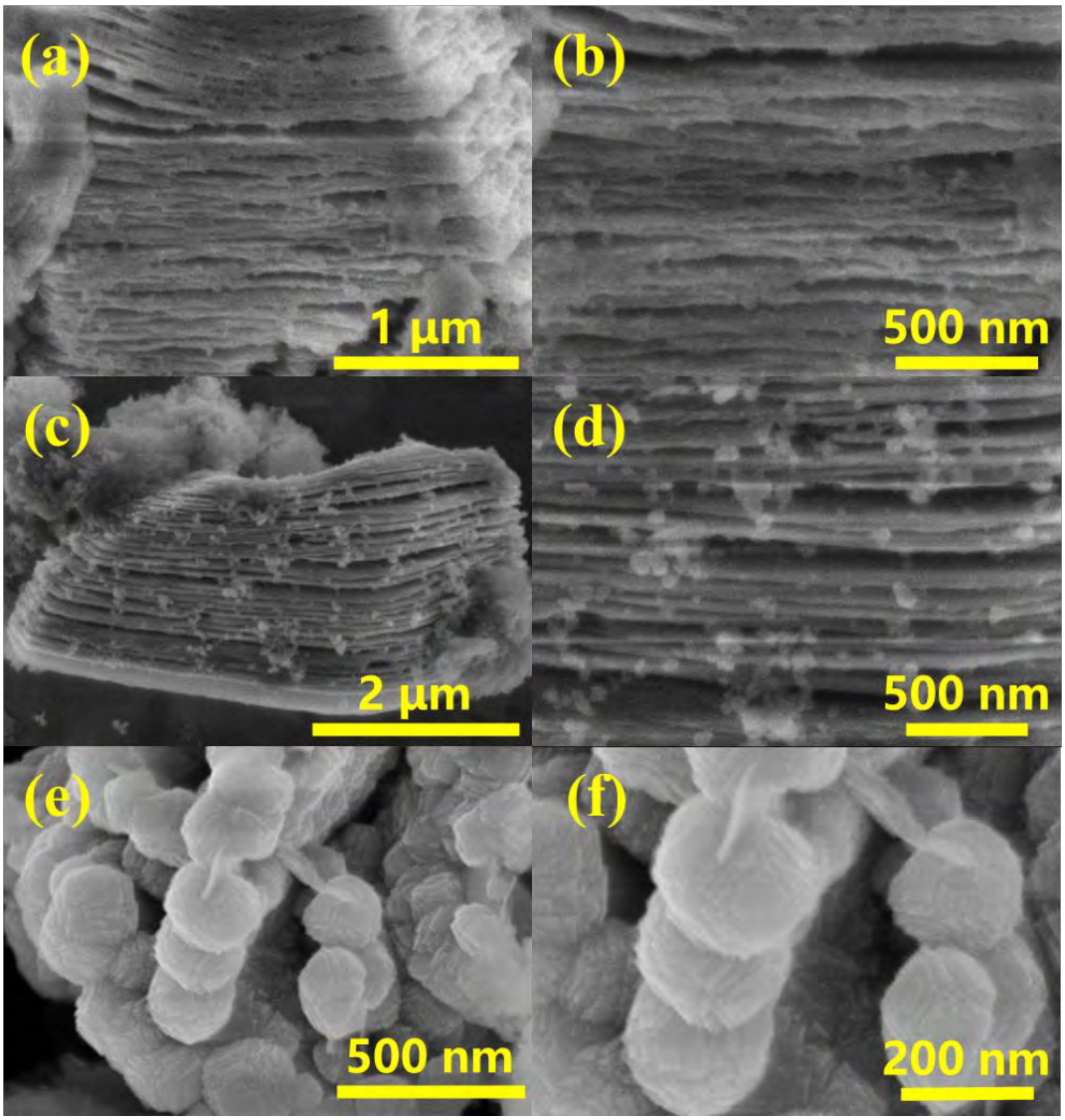

Fig. S1. Surface SEM images of (a) and (b) $Co_1Ga_{0.5}$-LDH/MXene; (c) and (d) Co_1Ga_0-LDH/MXene; (e) and (f) Co-LDH.

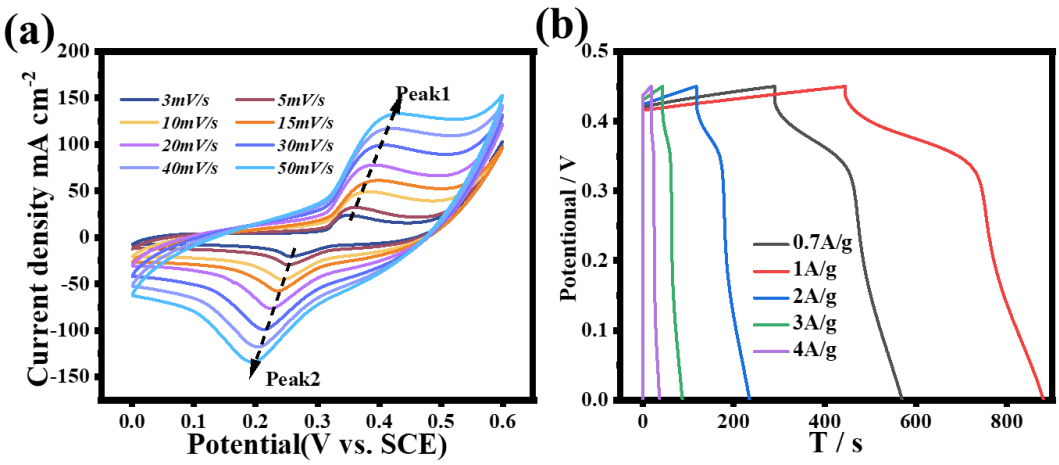

Fig. S2. (a) CV curves of $Co_1Ga_{0.5}$-LDH/MXene at different scanning rates and (b) GCD curves of $Co_1Ga_{0.5}$-LDH/MXene for different current densities.

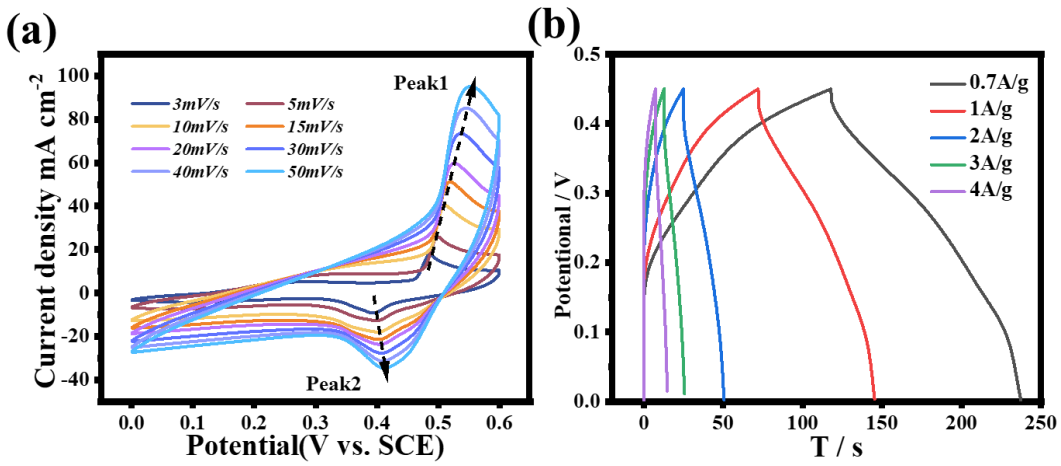

Fig. S3. (a) CV curves of Co_1Ga_0-LDH/MXene at different scanning rates and (b) GCD curves of Co_1Ga_0-LDH/MXene for different current densities.

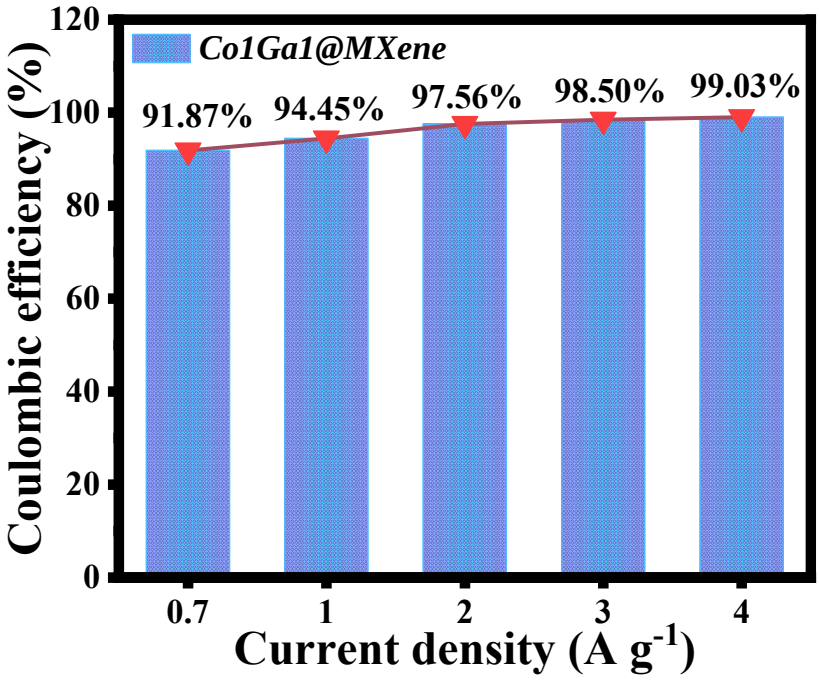

Fig. S4. Coulombic efficiency of Co_1Ga_1-LDH/MXene for different current densities.

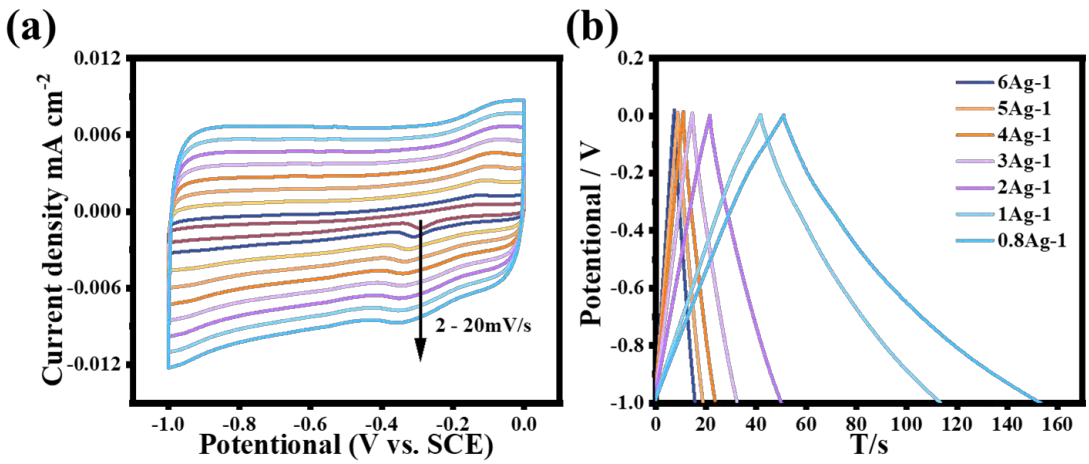

Fig. S5. (a) CV curves of activated carbon at different scanning rates and (b) GCD curves of activated carbon for different current densities.

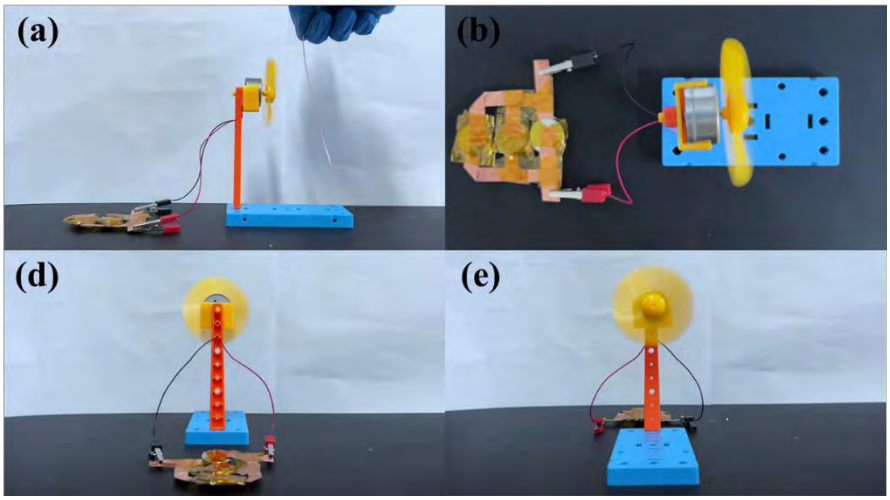

Fig. S6. ACS integrator powering small fan with lithium battery: (a) side view; (b) top view; (b) rear view; (b) front view.

Table S1. electrochemical properties of MXene-based composites [1-5].

S.No	Materials	Capacity/capacitance	Capacity-capacitance-retention / Cycle numbers (% cycles)
1	S-MXene/HG	446 F g^{-1} at 2 mV s^{-1}	96/10,000
2	MXene-N	286.28 F g^{-1} at 3 A g^{-1}	98/10,000
3	P-MXene/CPAQ-A	532.9 F g^{-1} at 1 A g^{-1}	82/1,000
4	$Ti_3C_2T_x$/APP-A	597.8 F g^{-1} at 5 mV s^{-1}	97.1/40,000

Table S2. electrochemical properties of LDH-based composites.

No.	Materials	Capacity/capacitance	Capacity-capacitance-retention / Cycle numbers (% cycles)
1	CoFe-LDH	629 F g^{-1} at 1 A g^{-1}	-
2	NiMn-LDH	1183 C g^{-1} at 1 A g^{-1}	76/5,000
3	CoNiMg-LDH	1095.2 C g^{-1} at 1 A g^{-1}	82/1,000
4	holey 2D TiN/NiCo-LDH	2127 F g^{-1} at 10 mV s^{-1}	-
5	SCFs@PPy@NiCo-LDH	1705.6 F g^{-1} at 1 A g^{-1}	78.2/4,000

Table S3. electrochemical properties of LDH/MXene-based composites.

No.	Materials	Capacity/capacitance	Capacity-capacitance-retention / Cycle numbers (% cycles)
1	MXene/NiAl-LDH	1061 F g^{-1} at 1 A g^{-1}	70/4,000
2	MXene-Ni-Co-LDH	983.6 F g^{-1} at 2 A g^{-1}	76/5,000
3	MXene-CTAB/NiCo-LDHs-DBS	1207 F g^{-1} at 0.5 A g^{-1}	93/5,000
4	$Ti_3C_2T_x$/Ni-Co-Al-LDH	748.2 F g^{-1} at 1 A g^{-1}	97.8/10,000
5	NiMn-LDH/MXene	1575 F g^{-1} at 0.5 A g^{-1}	91.8/10,000

References

[1] Z. Cai, Y.F. Ma, M. Wang, A.N. Qian, Z.M. Tong, L.T. Xiao, S.T. Jia, X.Y. Chen, Engineering of electrolyte ion channels in MXene/holey graphene electrodes for superior supercapacitive performances, Rare Metals 41(6) (2022) 2084-2093.http://dx.doi.org/10.1007/s12598-021-01935-6.
[2] K. Nasrin, V. Sudharshan, K. Subramani, M. Sathish, Insights into 2D/2D MXene Heterostructures for Improved Synergy in Structure toward Next-Generation Supercapacitors: A Review, Advanced Functional Materials 32(18) (2022).http://dx.doi.org/10.1002/adfm.202110267.
[3] L.Y. Pu, J.X. Zhang, N.K.L. Jiresse, Y.F. Gao, H.J. Zhou, N. Naik, P. Gao, Z.H. Guo, N-doped MXene derived from chitosan for the highly effective electrochemical properties as supercapacitor, Advanced Composites and Hybrid Materials 5(1) (2022) 356-369.http://dx.doi.org/10.1007/s42114-021-00371-5.
[4] Y.F. Liang, H.L. Shen, J.H. Li, H.Y. Zhao, J.H. Xu, H.F. Huang, S.K. Xu, X.Q. Liang, W.Z. Zhou, J. Guo, Tailoring surface terminals of Ti₃C₂Tx MXene microgels via interlayer domain-confined polyphosphate ammonium for flexible supercapacitor applications, Chemical Engineering Journal 497 (2024).http://dx.doi.org/10.1016/j.cej.2024.154775.
[5] C. Jing, S.R. Tao, B. Fu, L. Yao, F.L. Ling, X.L. Hu, Y.X. Zhang, Layered double hydroxide-based nanomaterials for supercapacitors and batteries: Strategies and mechanisms, Progress in Materials Science 150 (2025).http://dx.doi.org/10.1016/j.pmatsci.2024.101410.